



National Library
of Canada

Bibliothèque nationale
du Canada

Acquisitions and
Bibliographic Services Branch

Direction des acquisitions et
des services bibliographiques

395 Wellington Street
Ottawa, Ontario
K1A 0N4

395, rue Wellington
Ottawa (Ontario)
K1A 0N4

Your file votre référence

Our file Notre référence

NOTICE

The quality of this microform is heavily dependent upon the quality of the original thesis submitted for microfilming. Every effort has been made to ensure the highest quality of reproduction possible.

If pages are missing, contact the university which granted the degree.

Some pages may have indistinct print especially if the original pages were typed with a poor typewriter ribbon or if the university sent us an inferior photocopy.

Reproduction in full or in part of this microform is governed by the Canadian Copyright Act, R.S.C. 1970, c. C-30, and subsequent amendments.

AVIS

La qualité de cette microforme dépend grandement de la qualité de la thèse soumise au microfilmage. Nous avons tout fait pour assurer une qualité supérieure de reproduction.

S'il manque des pages, veuillez communiquer avec l'université qui a conféré le grade.

La qualité d'impression de certaines pages peut laisser à désirer, surtout si les pages originales ont été dactylographiées à l'aide d'un ruban usé ou si l'université nous a fait parvenir une photocopie de qualité inférieure.

La reproduction, même partielle, de cette microforme est soumise à la Loi canadienne sur le droit d'auteur, SRC 1970, c. C-30, et ses amendements subséquents.

UNIVERSITY OF ALBERTA

**THE ACCELERATION OF A SINGLE BUBBLE RISING
FROM A NOZZLE IN WATER**

BY



BO JIANG

A thesis submitted to the Faculty of Graduate Studies and Research in partial fulfillment
of the requirements for the degree of MASTER OF SCIENCE.

DEPARTMENT OF MECHANICAL ENGINEERING

EDMONTON, ALBERTA

FALL 1992



National Library
of Canada

Bibliothèque nationale
du Canada

Canadian Theses Service Service des thèses canadiennes

Ottawa, Canada
K1A 0N4

The author has granted an irrevocable non-exclusive licence allowing the National Library of Canada to reproduce, loan, distribute or sell copies of his/her thesis by any means and in any form or format, making this thesis available to interested persons.

The author retains ownership of the copyright in his/her thesis. Neither the thesis nor substantial extracts from it may be printed or otherwise reproduced without his/her permission.

L'auteur a accordé une licence irrévocable et non exclusive permettant à la Bibliothèque nationale du Canada de reproduire, prêter, distribuer ou vendre des copies de sa thèse de quelque manière et sous quelque forme que ce soit pour mettre des exemplaires de cette thèse à la disposition des personnes intéressées.

L'auteur conserve la propriété du droit d'auteur qui protège sa thèse. Ni la thèse ni des extraits substantiels de celle-ci ne doivent être imprimés ou autrement reproduits sans son autorisation.

ISBN 0-315-77126-7

Canada

UNIVERSITY OF ALBERTA
RELEASE FORM

NAME OF AUTHOR: **BO JIANG**

TITLE OF THESIS: **THE ACCELERATION OF A SINGLE BUBBLE
RISING FROM A NOZZLE IN WATER**

DEGREE: **MASTER OF SCIENCE**

YEAR THIS DEGREE GRANTED: **FALL 1992**

Permission is hereby granted to the University of Alberta Library to reproduce single copies of this thesis and to lend or sell such copies for private, scholarly or scientific research purposes only.

The author reserves all other publication and other rights in association with the copyright in the thesis, and except as hereinbefore provided neither the thesis nor any substantial portion thereof may be printed or otherwise reproduced in any material form whatever without the author's prior written permission.

Bo Jiang

Permanent Address:

Bo Jiang

Drilling Research Institute

Sheng Li Oilfield

Dong Ying, Shan Dong, China

Date: Oct. 14, 1992

SEP 11 1992

Bo Jiang
Dept. of Mechanical Engineering
University of Alberta
Edmonton, Alberta
Canada T6G 2G8

Permission Department
ACADEMIC PRESS, INC.
1250 Sixth Avenue
San Diego, California 92101
U.S.A.

September 1st, 1992

Dear Sir:

I am writing to you to ask your permission to include a figure in my M.Sc. thesis. The figure is in page 27 (Figure 2.5) of the book entitled "Bubbles, Drops, and Particles" by Clift, Grace and Weber (1978).

I would be grateful if permission is granted to use the figure in my thesis. Thank you.

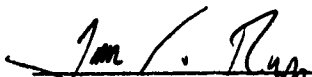
Yours Sincerely,

Bo Jiang
Bo Jiang

PLEASE TURN OVER

September 15, 1992

PERMISSION GRANTED, provided that 1) complete credit is given to the source, including the Academic Press copyright notice; 2) the material to be used has appeared in our publication without credit or acknowledgement to another source and 3) if commercial publication should result, you must contact Academic Press again.

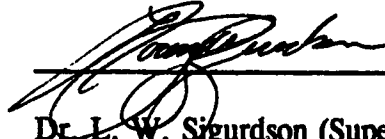


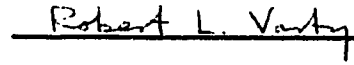
Martha Strassberger
Contracts, Rights and Permissions
ACADEMIC PRESS, INC.
Orlando, FL 32887


UNIVERSITY OF ALBERTA

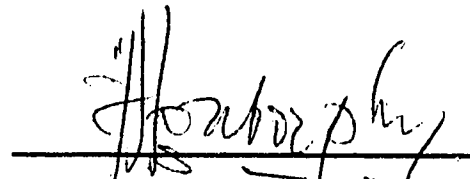
FACULTY OF GRADUATE STUDIES AND RESEARCH

The undersigned certify that they have read, and recommend to the Faculty of Graduate Studies and Research for acceptance, a thesis entitled **THE ACCELERATION OF A SINGLE BUBBLE RISING FROM A NOZZLE IN WATER** submitted by **BO JIANG** in partial fulfillment of the requirements for the degree of **MASTER OF SCIENCE**.



Dr. L. W. Sigurdson (Supervisor)

Dr. R. L. Varty

Dr. T. W. Forest

Dr. N. O. Egiebor

Date: Oct. 13, 1992

ABSTRACT

The study deals with the initial motion of a single bubble rising from rest in water. Both experimental and theoretical work were carried out. The volume-equivalent diameters of the bubbles studied were in the range from 0.59 mm to 1.23 mm. Bubbles of this size travelled rectilinearly. The corresponding instantaneous Reynolds number varied from approximately 0 to about 400, and the Eötvös number varied from 0.05 to 0.21.

The experiments were conducted in a vertical Plexiglas column filled with distilled water. The column had a square cross section of 100 mm by 100 mm and a height of 600 mm. The bubbles were generated by injecting air through a nozzle which was located at the bottom of the column. The bubble rising velocities were measured using a dual-beam, forward-scatter-mode, laser-Doppler anemometer at varying distances directly above the nozzle. The volume-equivalent diameter of the bubble was measured by photography. The bubble generating frequency was controlled to be around one Hz by adjusting the air pressure through a regulator.

It was found that the bubble rising velocity increased with the height very rapidly in the earlier stage and then more gradually until a maximum velocity was reached. The bubble rising velocity decreased slightly with the distance afterwards.

Theoretical work was also carried out to predict the bubble acceleration based on the assumptions that the bubble had a spherical shape and a constant volume. The drag force, which included the quasi-steady term and the added-mass term, was carefully evaluated in order to solve the governing equation. A semi-empirical (quasi-steady) drag coefficient was obtained using the experimentally obtained maximum bubble rising velocity in the present study. The semi-empirical drag coefficient was subsequently used to predict the bubble acceleration. A theoretical model that describes the motion worked quite well. Dimensionless groups were developed which correlate quite well the bubble rising velocity with distance for all the bubble sizes used in the present work.

ACKNOWLEDGEMENTS

The author would like to thank her former supervisor, Dr. R. L. Varty for his introducing her to this field and for financial support through the Natural Sciences and Engineering Research Council of Canada, grant number OGP0006015. His guidance, patient and continual interest in the project are appreciated. The author would also like to thank her later supervisor, Dr. L. W. Sigurdson for helpful discussions, suggestions and encouragement and for financial support through the Natural Sciences and Engineering Research Council of Canada, grant number OGP0041747.

Thanks are also due to the members of Mechanical Engineering Technical Staff for their help and some fellow graduate students for their help.

Finally, the author would like to express special thanks to her parents for their inspiration throughout her entire education and her husband Huhua Yan for his love, encouragement and technical discussion.

TABLE OF CONTENTS

CHAPTER 1 INTRODUCTION	1
1.1 Need to Study Single-Bubble Motion	1
1.2 Single-Bubble Motion	1
1.3 Objectives	2
1.4 Organization of the Thesis	2
 CHAPTER 2 THEORY OF SINGLE-BUBBLE MOTION ABOVE A	
NOZZLE	4
2.1 Reynolds Number, Eötvös Number, Weber Number and Froude Number	4
2.2 Bubble Motion Equation	5
2.3 Steady Motion at a Low Reynolds Number	8
2.4 Steady Motion at a Higher Reynolds Number	9
2.5 Accelerated Motion at low Reynolds Numbers	11
2.6 Accelerated Motion at Higher Reynolds Numbers	12
2.7 Summary	14
 CHAPTER 3 APPARATUS AND PROCEDURE	16
3.1 Introduction	16
3.2 Flow Column	16
3.3 Laser-Doppler Anemometer	16
3.3.1 Introduction	17
3.3.2 Velocity Measurements	17
3.4 Bubble Size Measurement by Taking Photographs	18
 CHAPTER 4 RESULTS AND DISCUSSION	23
4.1 Variation of Bubble Rising Velocity with Distance above the Nozzle	23
4.2 Effects of Bubble Generating Frequency	24

4.3 Accuracy of Temperature Measurement	24
4.4 Experiment Repeatability	25
4.5 Terminal Velocity (Maximum Velocity)	25
4.6 Theoretical Prediction	26
4.7 Evaluation of a New C_D Form from the Present Experiments	27
4.8 Discussion of the Added-Mass Coefficient	28
4.9 Variation of the Quasi-Steady Drag Force and the Added-Mass Force with Distance	28
4.10 Discussion on Bubble Shape	30
4.11 Non-Dimensional Representation of the Data and Correlations	30
 CHAPTER 5 CONCLUSIONS	 49
 REFERENCES	 50
 APPENDIX A NOZZLE MAKING	 52
 APPENDIX B TESTING THE LASER-DOPPLER ANEMOMETER	 54
B.1 Testing the Opto-Electronic System	54
B.2 Testing the Signal-Processing Program	54
B.3 Bubble Size Measurement Using LDA	55
B.3.1 Introduction	55
B.3.2 Theories	55
B.3.2.1 The Fringe Method of Particle Sizing	55
B.3.2.2 Sellens' theory	57
B.3.3 Experimental Apparatus	60
B.3.4 The Testing Results	60
B.3.4.1 Fringe Spacing	60
B.3.4.2 Signal Properties and Bubble Size	61
 APPENDIX C DETERMINATION OF THE DIMENSIONLESS GROUPS	 71

LIST OF TABLES

Table B.3.1 Comparison of fringe spacing between theory and measurement.....	61
Table B.3.2 Comparison of signal properties between theories and measurement and comparison of bubble sizes calculated from two different theories with the known model bubble size for the radius $a=2.36$ mm.....	62
Table B.3.3 Comparison of signal properties between theories and measurement and comparison of bubble sizes calculated from two different theories with the known model bubble size for the radius $a=4.36$ mm.....	62
Table B.3.4 Comparison of signal properties between theories and measurement and comparison of bubble sizes calculated from two different theories with the photographically measured bubble sizes.....	63

LIST OF FIGURES

Figure 1.1 Bubble formation and bubble rising velocity.	3
Figure 2.1 Shape regimes for bubbles and drops in unhindered gravitational motion through liquids (Clift et al., 1978).	15
Figure 3.1 Flow column and laser-Doppler anemometer for the bubble rising velocity measurement.	19
Figure 3.2 Optical system of the dual-beam forward scattering LDA.	20
Figure 3.3 The principle of the bubble rising velocity measurement using LDA.	21
Figure 3.4 Bubble size measurement by photography.	22
Figure 4.1 Variation of bubble rising velocity with distance above the nozzle for different bubble sizes.	32
Figure 4.2 Effect of bubble generating frequency on bubble rising velocity for two different bubble sizes.	33
Figure 4.3 Variation of room temperature and water temperature with time.	34
Figure 4.4 Effect of temperature variation on bubble rising velocity.	35
Figure 4.5 Test of experiment repeatability, (a) $D_e=0.67$ mm, (b) $D_e=1.10$ mm.	36
Figure 4.6 Comparison of the maximum bubble rising velocity between the present study and the literature results.	37
Figure 4.7 Prediction of the bubble rising velocity using different C_D forms at $\Delta_A=1.0$	38
Figure 4.8 Evaluation of the steady drag coefficient based on the maximum bubble rising velocity.	40
Figure 4.9 Comparison between the experimental data and the predictions for the bubble rising velocity using the new C_D at $\Delta_A=1.0$	41
Figure 4.10 Effect of the added-mass coefficient at different values on the prediction of bubble rising velocity	43
Figure 4.11 Variation of the quasi-steady drag force and the added-mass force with distance.	45

Figure 4.12 Variation of total drag force with distance.	45
Figure 4.13 Variation of the bubble aspect ratio with distance.	46
Figure 4.14 Variation of the volume-equivalent bubble diameter with distance.	47
Figure 4.15 Variation of the dimensionless velocity with the dimensionless distance.	48
Figure A.1 The process of the pulling of the nozzle tip.	53
Figure B.1.1 Variation of the model air bubble rising velocity (calculated from the rotating speed of the disk) with the model air bubble rising velocity (measured from the LDAVEL program).	65
Figure B.2.1 Variation of the model air bubble rising velocity (calculated from the signal frequency) with the model air bubble rising velocity (measured from the LDAVEL program).	66
Figure B.3.1 (a) Two crossing laser beams passing through a bubble, (b) received by a photodetector pair.	67
Figure B.3.2 (a) Two reference beams passing through a bubble in water, (b) scattering by refraction in a bubble.	68
Figure B.3.3 Flow column and laser-Doppler anemometer for bubble size measurement.	69
Figure B.3.4 Variation of time delay with photodiode orientation (turning angle).	70

NOMENCLATURE

a	bubble radius
A_{ij}	striking angle
B_{ij}	angle between sending beam i and scattering beam j
C_D	drag coefficient
d_f	fringe spacing
D_b	spherical bubble diameter
D_e	volume-equivalent spherical bubble diameter $(6V/\pi)^{1/3}$
D_y	bubble diameter in long axis
D_z	bubble diameter in short axis
Eo	Eotvos number
f	bubble generating frequency
f_d	drag force per volume
f_D	Doppler frequency
f_{o1}	frequency of sending beam 1
f_{o2}	frequency of sending beam 2
f_{i1}	frequency of scattering beam 1
f_{i2}	frequency of scattering beam 2
F_D	drag force
F_{Ds}	quasi-steady drag
F_{DA}	added-mass drag
F_{DH}	history drag

Fr	Froude number
g	gravitational acceleration
L	distance between the centre of the sphere and a photodetector
m	refractive index of spheres relative to surrounding medium
M	Morton number
M_A	acceleration modulus
n_c	refractive index of continuous phase
n_d	refractive index of dispersed phase (bubble)
p	liquid pressure
Re	Reynolds number
R^*	dimensionless radius of bubbles
S	effective distance between two photodetectors
S_o	distance between two photodetectors
t	time
T_D	signal period
T_s	time required for a fringe moving from one detector to another
V	bubble volume or dimensional velocity
V_{dis}	velocity of model air bubble on the edge of a rotating disk
V_f	fringe moving velocity
V_{pro}	velocity determined from the program LDAVEL
V_{osc}	velocity calculated from the display of the oscilloscope
V^*	dimensionless velocity of bubbles
U_b	bubble rising velocity

U_{br}	terminal velocity of a rising bubble
U_L	average liquid velocity
U_s	velocity of solid spheres
We	Weber number
Z_b	distance between a bubble and the tip of a nozzle
x,y,z	coordinate system
α_w	half angle of sending beam intersection in water
α	half angle of sending beam intersection in vacuum
β_w	half angle of receiving beam intersection in water
Δ_A	added-mass coefficient
$\Delta\phi_{12}$	phase shift between two Doppler signals (1 and 2)
Δ_H	history coefficient
ΔL_{ij}	length difference between refracted path length and reference path length (i sending beam, j scattering beam)
$\Delta\rho$	density difference between liquid and gas ($\rho-\rho_b$)
λ	beam wavelength in vacuum
μ	viscosity of liquid
ν	kinematic viscosity of liquid
ρ	density of liquid
ρ_b	density of gas
σ	surface tension of liquid-gas interface

θ scattering angle

θ_0 angle of the whole photodetector turning from horizontal plane

CHAPTER 1 INTRODUCTION

1.1 Need to Study Single-Bubble Motion

Bubbles are an indispensable part of a host of industrial and man-related activities. They can be found in many of the applications and play an important role in many natural physical processes encountered in mechanical, chemical, civil, metallurgical and food engineering, such as, boiling, electromachining, distillation, absorption, flotation, antibiotic fermentation, food processing and beer-making to name a few. Bubble motion in a liquid is also an area of fundamental interest in the study of two-phase gas/liquid flow. Although in general any of the above mentioned physical processes involve many bubbles, it is essential to first understand the motion of a single bubble in order to improve our understanding of the whole phenomenon. Therefore, in this study, we will focus our attention on a single air bubble rising from a nozzle in water.

1.2 Single-Bubble Motion

Single-bubble motion has been studied extensively. Basically, the rising of a bubble from a nozzle can be classified into three stages (see figure 1.1).

The first stage is the bubble formation where a bubble grows in size as gas blows from the nozzle. At a critical size, the bubble detaches from the tip of the nozzle and rises up. This critical bubble volume is determined by a force balance between the buoyant force and the surface tension force. In this stage, the bubble rising velocity U_b is approximately zero.

The second stage of a bubble rising is the bubble acceleration. In this stage, the bubble rising velocity increases with time or distance until it reaches its terminal velocity. The force balance between buoyant force, drag force and inertial force determines the acceleration.

After achieving the terminal velocity, the bubble rises with a constant velocity¹

¹The variation of the rising velocity after achieving the maximum value will be further discussed later (section 4.1).

which is the third stage of a bubble rising from a nozzle. In the third stage, the buoyant force is equal to the drag force.

The bubble formation and the terminal velocity have been well studied (Clift et al. 1978, Wallis 1969, 1974). However the acceleration stage has not been well investigated. Therefore, in the present study, we will deal with the acceleration of a bubble.

1.3 Objectives

The theory for the acceleration of a bubble has limitations and experimental study has been scarce. Therefore, the objectives of this study are first of all to measure experimentally the accelerating bubble velocity; secondly to find a suitable mathematical model to predict the velocity. Drag force plays an important role in bubble motion; therefore, it is very important to evaluate the drag force. There are some experimental correlations and theories for the drag force, but they are only applicable in special situations.

1.4 Organization of the Thesis

The first chapter is the general introduction to the thesis. Chapter 2 discusses the theory of the single-bubble motion. Relevant non-dimensional groups, such as Reynolds number, Eotvos number, Weber number and Froude number are introduced and discussed. Both the steady motion and the accelerated motion at low and higher Reynolds numbers are reviewed. Chapter 3 describes the experimental apparatus and the procedure. The mechanism of the laser-Doppler anemometer for measuring bubble rising velocities is discussed. The procedure for bubble size measurements by taking photographs is also described. Chapter 4 presents the results and the discussion, and Chapter 5 summarizes the conclusions.

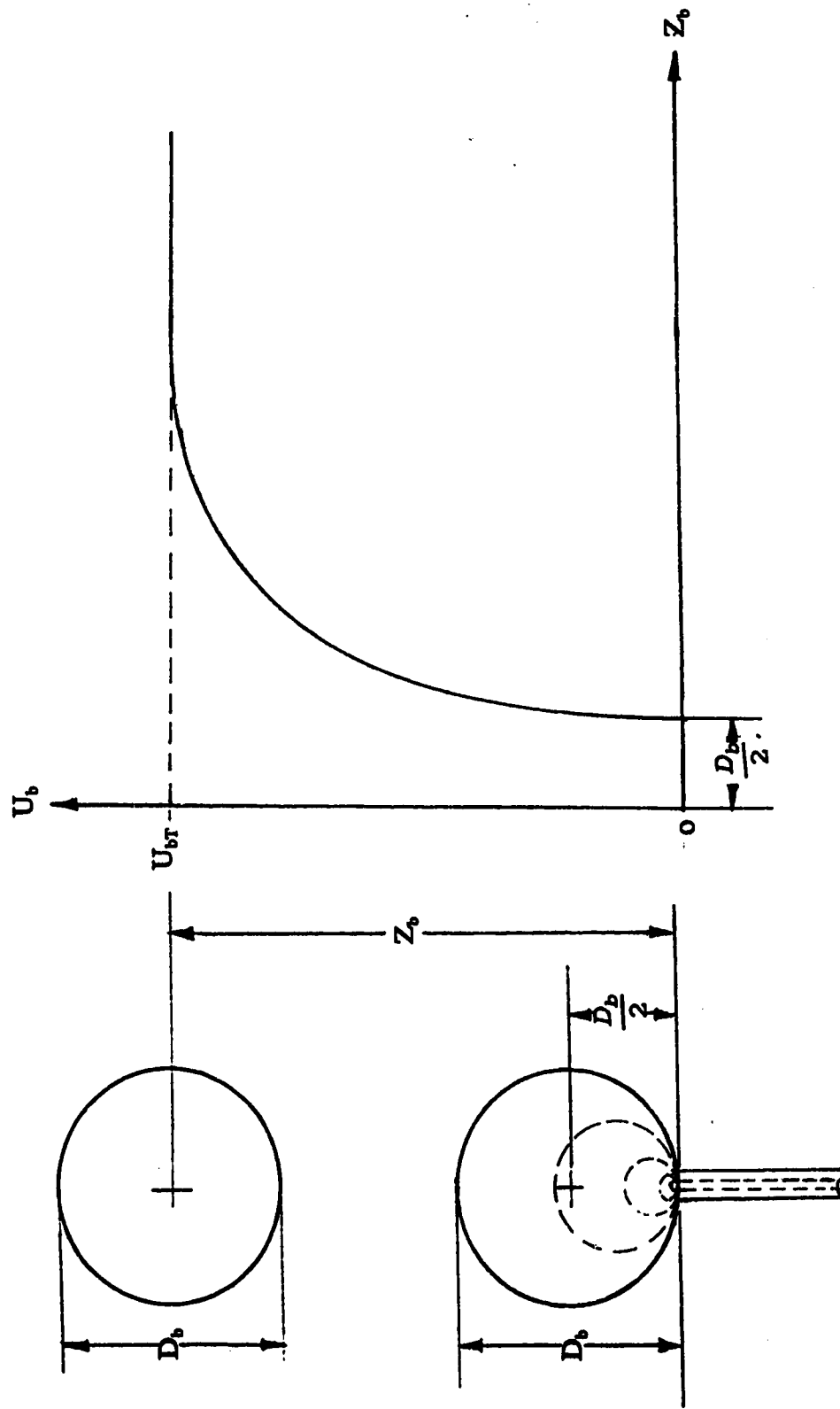


Figure 1.1 Bubble formation and bubble rising velocity.

CHAPTER 2 THEORY OF SINGLE-BUBBLE MOTION ABOVE A NOZZLE

2.1 Reynolds Number, Eötvös Number, Weber Number and Froude Number

In the area of bubbly flow, several dimensionless groups are often used. Therefore, it is desirable to discuss the physical significance of these groups before we proceed to detailed equations.

Reynolds number is defined as:

$$Re = \frac{\rho U_b D_b}{\mu}$$

where ρ is the density of liquid; U_b is the bubble rising velocity; D_b is the bubble diameter²; μ is the viscosity of the liquid.

The physical meaning of Reynolds number (Re) is the ratio of inertial force ($\propto \rho U_b^2 D_b^2$) to viscous force ($\propto \mu U_b D_b$). High Reynolds number flow means that inertial force is dominant and the viscous force can be neglected. Conversely, at low Reynolds numbers, the viscous force becomes significant and the inertia term can be neglected. Thus, Reynolds number is often used to characterize the relative importance of the inertia and the viscous forces.

The bubble shape is closely related to the surface tension, and the Eötvös and Weber numbers need to be introduced. They are defined as follows, respectively:

$$Eo = \frac{g D_b^2 \Delta \rho}{\sigma}$$

$$We = \frac{\rho U_b^2 D_b}{\sigma}$$

where g is gravitational constant; D_b is the bubble diameter; $\Delta \rho$ is the density difference between the liquid and the gas; σ is the surface tension of liquid-gas interface.

²In the present study, a volume-equivalent bubble diameter (D_e) is used which is calculated based on the bubble volume $\{D_e = (6V/\pi)^{1/3}\}$.

In the literature, both We and Eo are commonly used as independent variables for correlating shape parameters for fluid particles. The Eötvös number (Eo), which is also known as the Bond number and Laplace number, represents the ratio of buoyancy force ($\propto D_b^3 \Delta \rho g$) to surface tension force ($\propto \sigma D_b$). The Weber number (We) represents the ratio of inertia force ($\propto \rho U_b^2 D_b^2$) to surface tension force ($\propto \sigma D_b$). In a particular flow situation, only one of either the Eötvös number or the Weber number is needed to characterize the bubble shape.

Froude number is defined for bubbles and drops by Clift et al.(1978). We will define the Fr as:

$$Fr = \frac{\rho U_b^2}{\Delta \rho g D_b},$$

which is the square of that defined by Clift et al.(1978). It represents the ratio of inertial force($\propto \rho U_b^2 D_b^2$) to buoyancy force($\propto \Delta \rho g D_b^3$). It also takes another form for a free surface flow:

$$Fr = \frac{U_b^2}{gL},$$

where L is the characteristic length.

2.2 Bubble Motion Equation

Single bubbles rising in liquids have been studied theoretically for many years. They were investigated by classifying the flow as steady or unsteady, low Reynolds number ($Re < 1$) or higher Reynolds number ($Re > 1$). The motion of a bubble rising from a nozzle is unsteady before it reaches its terminal velocity (The terminal velocity is not a constant value which will be discussed later). The Reynolds number varies from zero to some constant value which depends on the bubble size, shape and the properties of the fluid. Therefore in this process both low Reynolds number and higher Reynolds number were involved. In this study, a spherical bubble rising rectilinearly is assumed.

Saffman (1956) found that rectilinear motion occurred when the diameter of a bubble was less than about 1.4 mm. Clift et al. (1978) showed that bubbles were nearly spherical at moderate Reynolds number ($Re = 500$) if surface tension forces are sufficiently strong. In figure 2.1, we can see that for a given Reynolds number, the bubble shape will be spherical when the Eötvös number is less than a critical value ($M = \text{Morton number} = (g\mu^4\Delta\rho)/(\rho^2\sigma^3)$) and will not be considered in this study). In this chapter, we deal with the cases for the bubble size in the range from 0.59 to 1.23 mm in diameter and the Reynolds number range from zero to about 400 and the Eötvös number from 0.05 to 0.21.

An unsteady bubble motion equation was obtained by Kuo and Wallis (1988). They applied the momentum equation for both phases, the bubble and the flowing liquid. The basic features of the equation development follows. The bubble was assumed to be infinitesimally small and therefore the average liquid motion was unaffected by the bubble. The equation of motion for a bubble moving in a flowing liquid in the vertical direction is:

$$\rho_b U_b \frac{dU_b}{dz} = -\frac{dp}{dz} - \rho_b g - f_d \quad (2.2.1)$$

where: ρ_b is the bubble density,

U_b is the bubble velocity,

p is the liquid pressure,

f_d is the drag force per volume,

z is the distance in the vertical direction.

The equation of motion for the surrounding liquid is:

$$\rho U_L \frac{dU_L}{dz} = -\frac{dp}{dz} - \rho g \quad (2.2.2)$$

where: ρ is the liquid density,

U_L is the average liquid velocity.

Combining equations (2.2.1) and (2.2.2) yields:

$$\rho_b U_b \frac{dU_b}{dz} = \rho U_L \frac{dU_L}{dz} + (\rho - \rho_b)g - f_d . \quad (2.2.3)$$

For a special case, where the surrounding fluid is stagnant, which is also true for our study, $U_L=0$. Also,

$$U_b \frac{dU_b}{dz} = \frac{dz}{dt} \frac{dU_b}{dz} = \frac{dU_b}{dt} . \quad (2.2.4)$$

Substituting equation (2.2.4) into equation (2.2.3) and multiplying by V (bubble volume) on both sides, we obtain:

$$\rho_b V \frac{dU_b}{dt} = \Delta \rho g V - F_D , \quad (2.2.5)$$

where the term on the left hand side of the equation is the rate change of inertia, and the first term on the right hand side of the equation is the buoyancy force. The last term (F_D) is the drag force on the bubble.

Equation (2.2.5) can also be obtained from equations given by Clift et al. (1978). It is simply Newton's second law. The drag force (F_D) is a difficult term to evaluate. In the literature, the drag force is described by:

$$F_D = F_{DS} + F_{DA} + F_{DH} . \quad (2.2.6)$$

F_{DS} is the so-called quasi-steady drag force term which is defined as:

$$F_{DS} = C_D \frac{\pi D_b^2 \rho}{8} U_b^2 , \quad (2.2.7)$$

where C_D is the drag coefficient. The quasi-steady term can be interpreted as the drag force which would exist for steady flow with a constant velocity U_b .

The second term F_{DA} is the added-mass term which accounts for the inertia of the liquid due to the acceleration of the bubble requiring the acceleration of the fluid. The

added mass is the mass of fluid which would be considered to move with the same velocity as the bubble, and models the fluid dynamic forces on the bubble due to its acceleration as an added inertia. It is a function of the rate of change of velocity and is defined as:

$$F_{DA} = \Delta_A \frac{\rho V dU_b}{2 dt} , \quad (2.2.8)$$

where ρ is the density of liquid, Δ_A is the added-mass coefficient and V is the bubble volume.

The last term is the history term which accounts for the history of the viscous flow (this term will be discussed in detail in sections 2.5 and 2.6.).

In the next few sections, the evaluation of the drag coefficient will be considered for different flow situations, steady and unsteady motion at both low and higher Reynolds numbers. The determination of the drag coefficient is not straightforward, because the drag coefficient is calculated from the flow field and the flow field surrounding a bubble has first to be calculated by solving the Navier-Stokes equations.

The preceding analysis is for a bubble rising in pure liquids. After a bubble reaches its maximum velocity, it will rise with a constant velocity. The effects of the liquid impurities on bubble rising velocity will be discussed in Chapter 4.

2.3 Steady Motion at a Low Reynolds Number

The Navier-Stokes equations can be used to describe the bubble flow, but the nonlinear terms in the equations make them very difficult to solve analytically. Therefore, some assumptions are often made to simplify the equation. One of them is the creeping flow approximation in which the convection term is neglected.

Consider a spherical bubble moving relative to a fluid of infinite extent with a steady velocity U_b . The Reynolds number is sufficiently low (Re less than 1) such that there is no wake at the rear of the bubble. The bubble is also assumed to be free from surface-active contaminants, and the interfacial surface tension is constant. The analytic solutions for this bubble flow were derived independently by Hadamard (1911) and

Rybczynski (1911) from the Navier-Stokes equations with the creeping flow approximation. The solutions were obtained in terms of the Stokes stream function for the fluids both inside and outside the bubble. The boundary conditions included: uniform stream flow at large distances from the sphere, no flow across the interface, continuity of tangential velocity across the interface and continuity of tangential stress across the interface. From the solution, they derived the overall drag coefficient (C_D) for a bubble. It is the sum of two contributions: the pressure drag over the surface of the bubble and the deviatoric normal stress. It has the form:

$$C_D = \frac{16}{Re} . \quad (2.3.1)$$

The terminal velocity (U_{bT}) of a bubble in creeping flow can be obtained by equating the total drag to the buoyancy force, giving:

$$U_{bT} = \frac{g\Delta\rho D_b^2}{12\mu} \quad (2.3.2)$$

where g is gravitational constant; μ is the viscosity of liquid; $\Delta\rho$ is the density difference between liquid and gas; D_b is the bubble diameter.

2.4 Steady Motion at a Higher Reynolds Number

The inertia term in the Navier-Stokes Equation can not be neglected at Reynolds numbers above one. Therefore, in this case the equation can be solved using one of the following methods: numerical simulation, error distribution method or boundary-layer approximations.

Numerical solutions give the most complete and probably the most reliable results (Clift et al. 1978). These solutions provide useful quantitative and qualitative information at intermediate Reynolds numbers (typically $Re < 300$). Numerical solutions from the Navier-Stokes equations in the form of the Stokes stream function for the flow around and inside fluid spheres are obtained using the finite difference method. The boundary

conditions are those described in section 2.3 for the Hadamard-Rybczynski solution. The numerical values of the drag coefficient were obtained by Brabston et al. (1975), Hamielec et al. (1967), and LeClair et al. (1971). An equation which fits the numerical values of the drag coefficient for spherical bubbles well was proposed by Haas et al. (1972):

$$C_D = 14.9Re^{-0.78} \quad (2 < Re < 1000) . \quad (2.4.1)$$

Hamielec et al. (1962, 1963) used the error distribution (or Galerkin) method for solving the Navier-Stokes equations. This method involves choosing a polynomial form for the stream function. This stream function was made such that all the boundary conditions are satisfied. Hamielec suggested a correlation for the drag coefficient for Reynolds numbers in the range of 4 to 100. For a gas bubble, the correlation takes the following form:

$$C_D = 13.73Re^{-0.74} \quad (4 < Re < 100) . \quad (2.4.2)$$

The boundary layer method is often used for flows with high Reynolds numbers. Viscous forces play a dominant role inside the boundary layer, while outside this layer the flow can be approximated as irrotational.

As a first approximation to irrotational flow, Levich (1962) calculated the viscous energy dissipation for potential flow past a fluid sphere. The drag coefficient is given by the following form:

$$C_D = \frac{48}{Re} \quad (Re > 50) . \quad (2.4.3)$$

The complete boundary layer equations were solved analytically by Moore (1963), but in the vicinity of the rear of the bubble, the velocity and pressure fields were found to have singularities. In calculating the energy dissipation, Moore also included the contributions from the boundary layer and wake. The improved drag coefficient is given by:

$$C_D = \frac{48}{Re} \left[1 - \frac{2.21}{Re^{-\frac{1}{2}}} + O(Re^{-\frac{5}{6}}) \right] \quad (Re > 50) . \quad (2.4.4)$$

2.5 Accelerated Motion at low Reynolds Numbers

Analytical solutions for unsteady motion of rigid and fluid spheres are available only in creeping flow. Basset (1888) considered the case for a solid sphere with zero slip velocity at the interface. A solution for a gas bubble with the no-tangential stress boundary condition was developed by Morrison and Stewart (1976). They also made a comparison between their solution and that of Basset for a solid sphere.

Morrison and Stewart's solution for a gas bubble was obtained by solving the Navier-Stokes equations with the creeping flow approximation. The resulting drag force is :

$$F_D = \frac{\rho}{2} V \frac{dU_b}{dt} + 2\pi\mu D_b U_b + \frac{6\rho V}{D_b} \sqrt{\frac{\nu}{\pi}} \int_{t_0}^t \frac{\frac{dU_b}{ds} ds}{\sqrt{t-s}} ds + \frac{\rho V D_b}{12\sqrt{\pi\nu}} \int_{t_0}^t \frac{d^2 U_b}{ds^2} \frac{ds}{\sqrt{t-s}} \quad (2.5.1)$$

where: t and s are time, $(t-s)$ is the time elapsed since the past acceleration, t_0 is the time at which the bubble begins to accelerate, and t is the present time.

The drag force on an accelerating solid sphere in a creeping flow by Basset(1888) is:

$$F_D = \frac{\rho}{2} V \frac{dU_s}{dt} + 3\pi\mu D_s U_s + \frac{9\rho V}{D_s} \sqrt{\frac{\nu}{\pi}} \int_{t_0}^t \frac{\frac{dU_s}{ds} ds}{\sqrt{t-s}} ds \quad (2.5.2)$$

where D_s is the diameter of a solid sphere and U_s is the velocity of a solid sphere.

Morrison and Stewart found that the first term on the right-hand side of the above

two equations (the added mass term) does not depend on the solid or fluid spheres, i.e., it only depends on the fluid density and bubble volume. They also found that the steady drag on the bubble is only $2/3$ of the Stokes drag on a rigid sphere represented by the second term on the right hand side of the above equations. We know that the Stokes drag coefficient for solid spheres is $24/Re$. Therefore, according to the above relation, the drag coefficient for a bubble is $16/Re$, which is exactly the drag coefficient for fluid spheres in creeping flow as discussed in section 2.3. The third term, which is called Basset term, or history term, has a value for gas bubbles which is $2/3$ of the that for solid spheres. It accounts for the history of the unsteady motion, integrating from the initial time t_0 , when the bubble starts from rest, to the present time t . The last term in equation (2.5.1) is the additional momentum diffusion term which is considered to be insignificant (Kuo & Wallis, 1988). Similar to the history term, it is an integral overtime. This term does not exist for a solid sphere. The above comparison reveals that the various terms in the drag force are very similar for the flow of a bubble and a solid sphere, differing only in their coefficients.

2.6 Accelerated Motion at Higher Reynolds Numbers

No known analytical solution exists for the full Navier-Stokes equations for unsteady single bubble motion at Reynolds numbers beyond one. Therefore numerical methods must be used. However, some simpler methods could be employed for this unsteady motion at higher Reynolds number. In the following, the methods for the case of a solid sphere will be discussed, and then applied to the case of a bubble.

Odar and Hamilton (1964) modified the drag force derived by Basset(1888) for creeping flow around rigid spheres. For higher Reynolds number flow, they added coefficients for both the added mass term and the history term to obtain the drag force. The drag force for creeping flow about a solid sphere is given by:

$$F_D = \frac{V\rho}{2} \frac{dU_s}{dt} + C_D \frac{\pi D_s^2 \rho}{8} U_s^2 + \frac{3D_s^2}{2} \sqrt{\pi \rho \mu} \int_{-\infty}^t \left(\frac{dU_s}{dt} \right)_{t-s} \frac{ds}{\sqrt{t-s}} \quad (2.6.1)$$

(which is equation 2.5.2). The drag force for higher Re is therefore:

$$F_D = \Delta_A \frac{V\rho}{2} \frac{dU_s}{dt} + C_D \frac{\pi D_s^2 \rho}{8} U_s^2 + \Delta_H \frac{3D_s^2}{2} \sqrt{\pi \rho \mu} \int_{-\infty}^t \frac{dU_s}{ds} \frac{ds}{\sqrt{t-s}} \quad (2.6.2)$$

where Δ_A and Δ_H are empirical coefficients by Odar and Hamilton which account for the differences from creeping flow. They are all a function of the acceleration modulus $M_A \{=(D_s/U_s^2)(dU_s/dt)\}$ (Clift et al., 1978).

As pointed out in Section 2.5, the terms in the drag force for the cases of a solid sphere and a bubble are very similar. Therefore, we could try to use the same form as equation (2.6.2) for the case of a bubble, with coefficients, C_D , Δ_A , Δ_H , that are to be different from those of a solid sphere.

Kuo and Wallis (1988) studied the accelerated motion of single bubbles injected into a liquid flow through a convergent- and-divergent nozzle. They also used the same form as equation (2.6.2) for the drag force, but only considered the quasi-steady drag term and the added mass term. They expected these two terms to be more significant than the history term. In their case, C_D was evaluated from their experimental results and correlations for C_D were developed. Three numerical values were tested for the added mass coefficient Δ_A , namely, $\Delta_A = 0, 1$ and 2 .

For a bubble rising from rest in stagnant water, an analytical solution for the bubble rising velocity was obtained by Varty (1991a). The quasi-static drag force and the added mass term were considered. The drag coefficient used was $C_D=48/Re$. The added mass coefficient was chosen to be one. It was found that for a bubble size of 1 mm in diameter the analytic solution gives a good prediction for the bubble rising velocities.

The present data has shown that for bubble sizes different than 1 mm (> 1 mm or < 1 mm), the prediction deteriorates. This will be discussed in Chapter 4.

2.7 Summary

The governing equation derived in Section 2.2 (equation 2.2.5) can only be solved when the total drag force is determined. For unsteady flow or accelerated motion, which we are concerned with in this study, the drag force can be split into several terms as we have discussed. The quasi-steady drag can be evaluated from solutions for steady flow. However, the determination of the added mass coefficient Δ_A is difficult from theoretical considerations, and a trial-and-error method has to be used. The history term is normally assumed to be unimportant and can be neglected for unsteady higher Reynolds number flow.

In Chapter 4, we shall solve the governing equation (2.2.5) to predict the bubble rising velocity. All the correlations discussed in Section 2.4 for C_D will be tested. A new correlation for C_D based on the terminal velocities of the rising bubble will be proposed and used in the governing equation. Different values for the added mass coefficient will also be used.

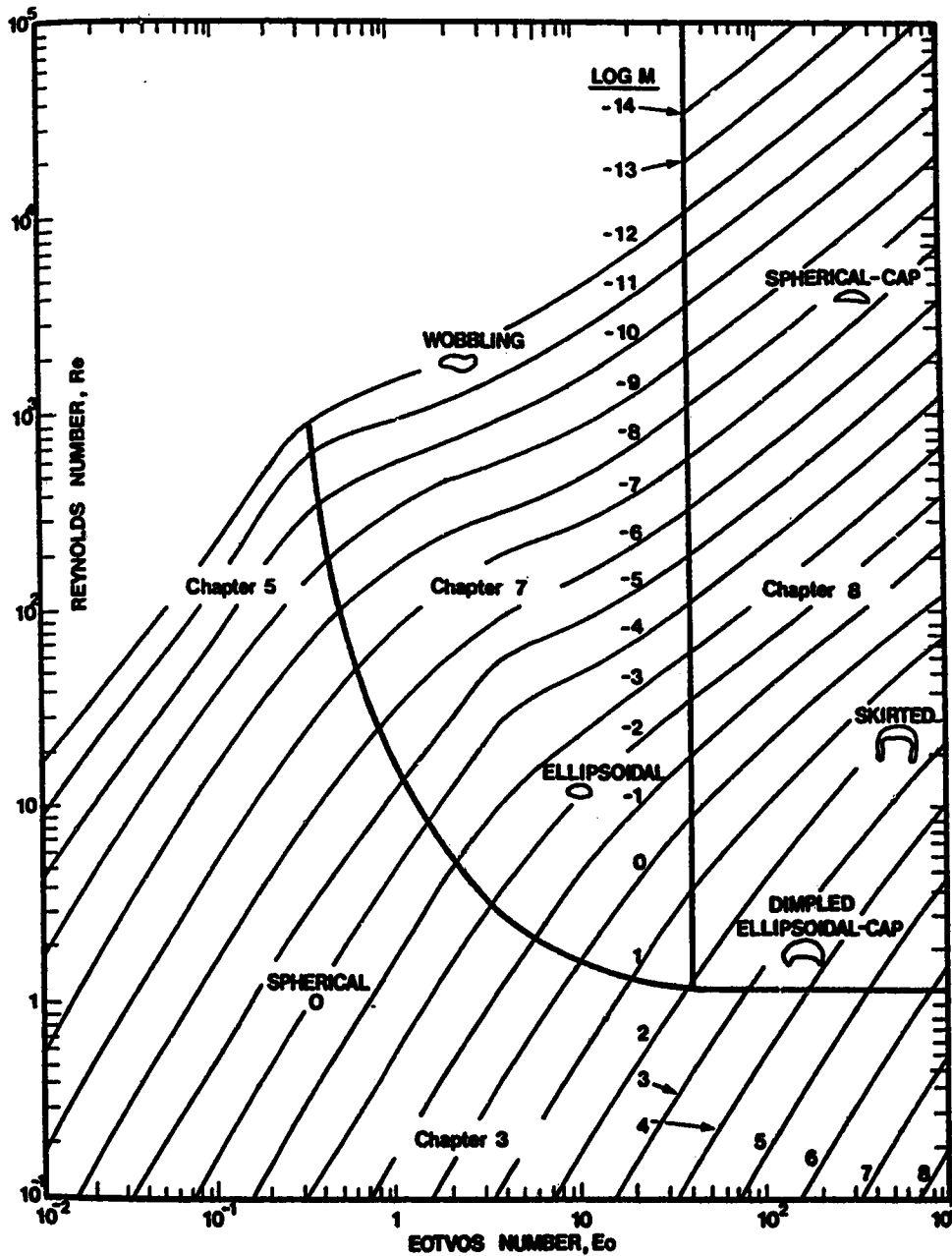


Figure 2.1 Shape regimes for bubbles and drops in un hindered gravitational motion through liquids (Clift et al., 1978).

CHAPTER 3 APPARATUS AND PROCEDURE

3.1 Introduction

Laser Doppler anemometry (LDA) has been used extensively for the flow measurements. The advantage of this method over others is that it does not introduce any probe disturbance to the flow. LDA was originally applied to velocity measurements in single-phase flows. Later, the use of this method was extended to the measurement of two-phase flows and also to the measurement of bubble size. In our experiments, the dual-beam forward-scatter LDA was used. In the next section, we will describe the test section, a flow column. The principles of velocity measurement using LDA will be discussed. Finally, bubble size measurement by taking photographs will be explained. This was used in the present study. Bubble size measurement using LDA will be described in Appendix B.3. It was found that during the calibration, this method did not give accurate bubble size measurement. Consequently, it was not used here.

3.2 Flow Column

The test section was a vertical Plexiglas column having a square cross section, which was mounted on a three-dimensional traversing mechanism. The schematic diagram of the flow column is shown in figure 3.1. The inside dimensions of the test section were 100 mm by 100 mm in the horizontal plane and 600 mm in the vertical direction. It was filled with distilled water. Air bubbles were injected through a nozzle located near the bottom of the column. The tip of the nozzle extended approximately 100 mm above the bottom of the test section. The procedure for making a nozzle is described in Appendix A. The bubble rising velocity from the moment it detaches from the nozzle until it reaches its terminal velocity was measured using the laser-Doppler anemometer. In order to measure the bubble rising velocity at different positions, the column can be moved up and down relative to the fixed laser-Doppler system using a motor.

3.3 Laser-Doppler Anemometer

3.3.1 Introduction

The LDA was operated in the dual-beam forward-scatter mode (see figure 3.1). The light source was a 10 mW helium-neon laser. The nominal wavelength λ in vacuum was 632.8 nm and the nominal e^{-2} beam diameter was 0.68 mm. The light passed through the transmitting optics into the flow column, and it was received by a photodetector. The signal from the photodetector went to a low pass-filter, and then to a digital storage oscilloscope. All the information from the oscilloscope was then stored in an HP computer. The bubble generation frequency was measured using a digital counter and a stop watch. The bubble generating frequency was controlled by adjusting the air pressure through a regulator.

The light from the laser passed through the two quarter wave plates which produce the vertical polarised light (figure 3.2). The polarised light was then split into two parallel beams by a prism. The focusing lens had a back focal length of 249.59 mm and a beam-crossing half angle α of 5.532° that was given by the manufacturer. The receiving optics consisted of a mask with an aperture diameter of 40 mm, a collecting lens with a front focal length of 254.6 mm, a scattered-light focusing lens with a back focal length of 120.7 mm, an iris with an aperture diameter of 2 mm, and a photodetector pair. More information about the LDA system can be found in Varty (1991b), e.g., signal processing and programming.

3.3.2 Velocity Measurements

Consider a bubble travelling with velocity U_b crosses the intersection of two laser beams perpendicularly, as shown in figure 3.3. Beam 1 and beam 2 which originally have the same frequency will be scattered to have different frequencies. The relationship between the frequency difference of the two scattered beams ($f_D = f_2 - f_1$) and the bubble crossing velocity obeys the following equation (Durst, 1982):

$$f_D = f_2 - f_1 = \frac{2U_b \sin \alpha}{\lambda} \quad (3.3.2.1)$$

where $\lambda (= 632.8 \times 10^{-9} \text{ m})$ is the beam wavelength in vacuum, and $\alpha (= 5.532^\circ)$ is the

half angle of the sending beam intersection in vacuum. This frequency difference is normally called the Doppler frequency, which is also the frequency of the signal caused by the interference fringe pattern moving on the photodetector. Therefore, by measuring the frequency of the interference fringe pattern, we can calculate the bubble crossing velocity U_b .

3.4 Bubble Size Measurement by Taking Photographs

Bubble size was measured from photographs. This technique also indicates how much the bubble shape deviates from a spherical shape.

Figure 3.4 shows how the pictures were taken. A camera was on one side of the flow column and a strobe-light was on the other side. It was difficult to take a still picture, because the bubble rises very fast. The strobe-light was necessary to freeze the image. The frequency of the strobe-light was adjusted to be the same or slightly faster than the bubble generating frequency. The 35mm negatives were normally enlarged 35 times and printed for measurement. The accuracy of the bubble size measurement is up to 1%.

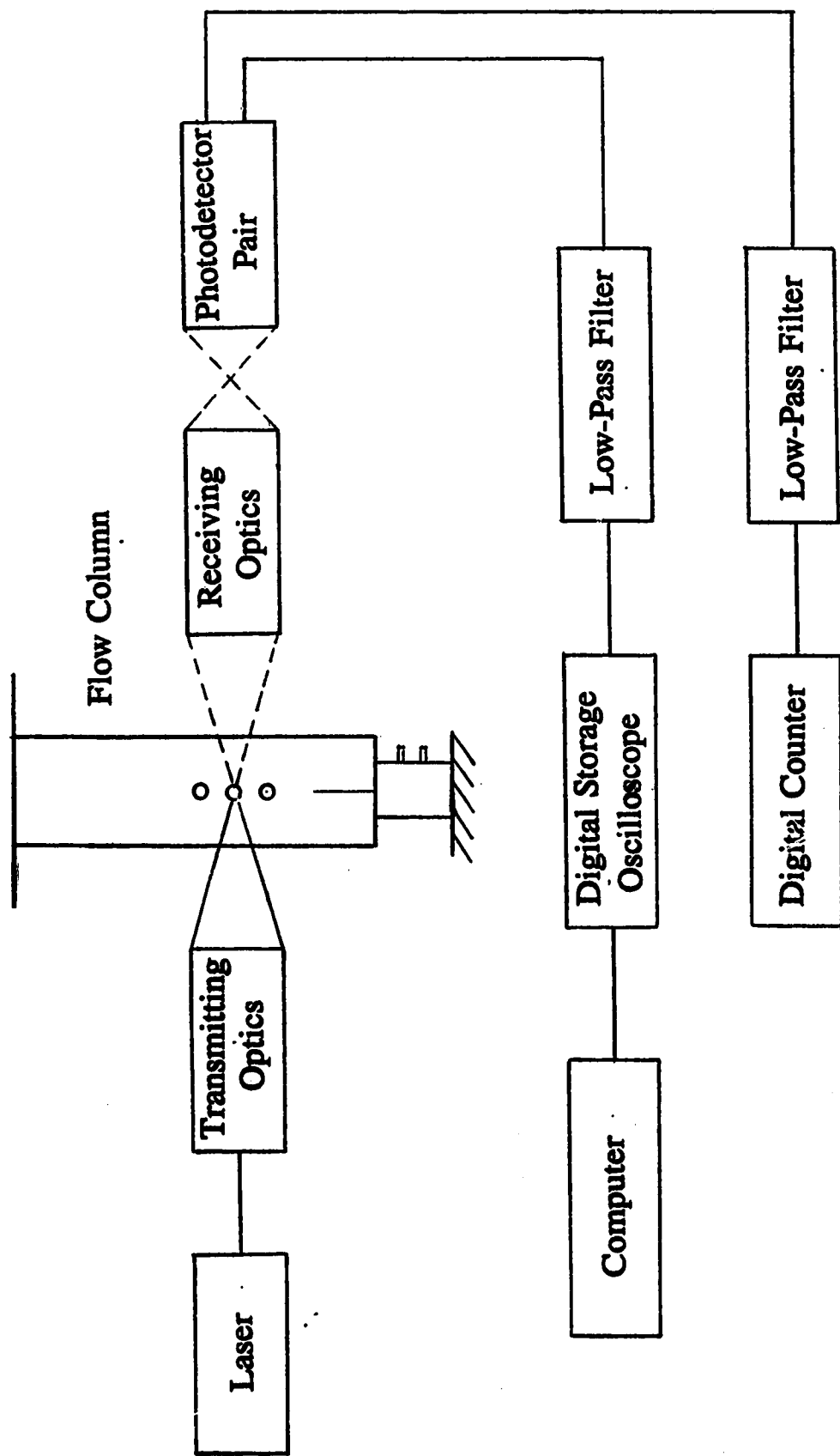


Figure 3.1 Flow column and laser-Doppler anemometer for the bubble rising velocity measurement.

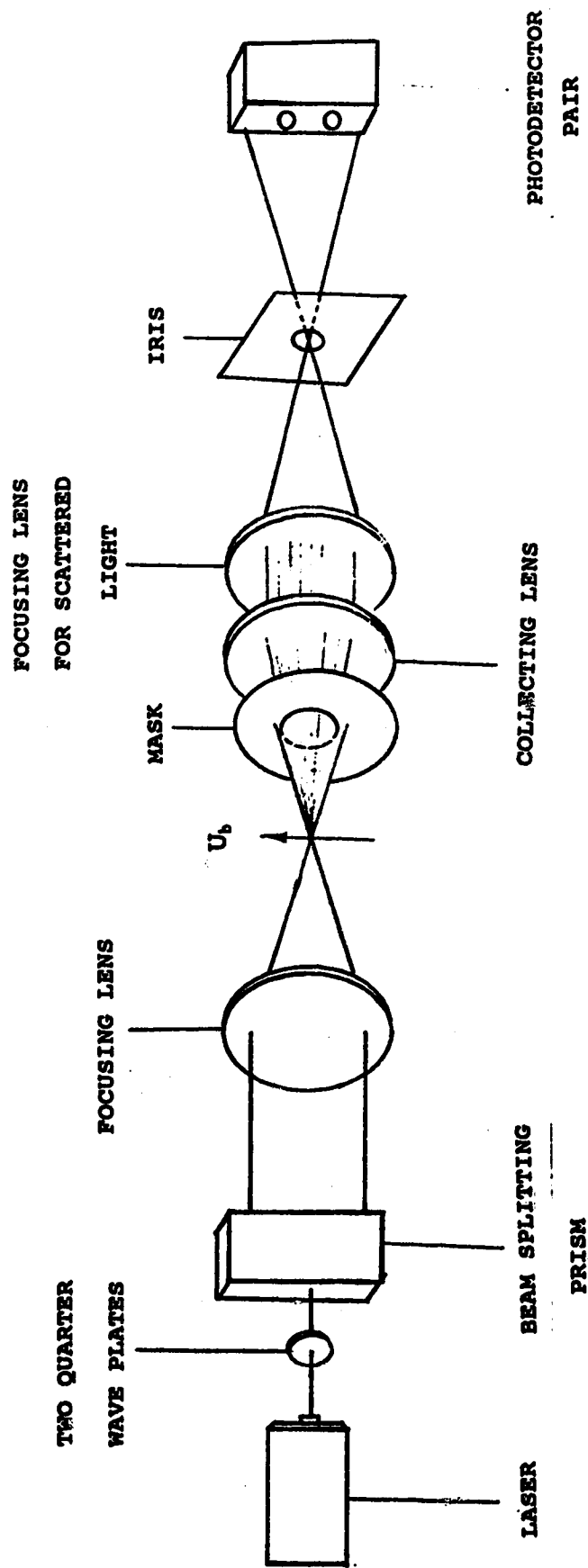


Figure 3.2 Optical system of the dual-beam forward scattering LDA.

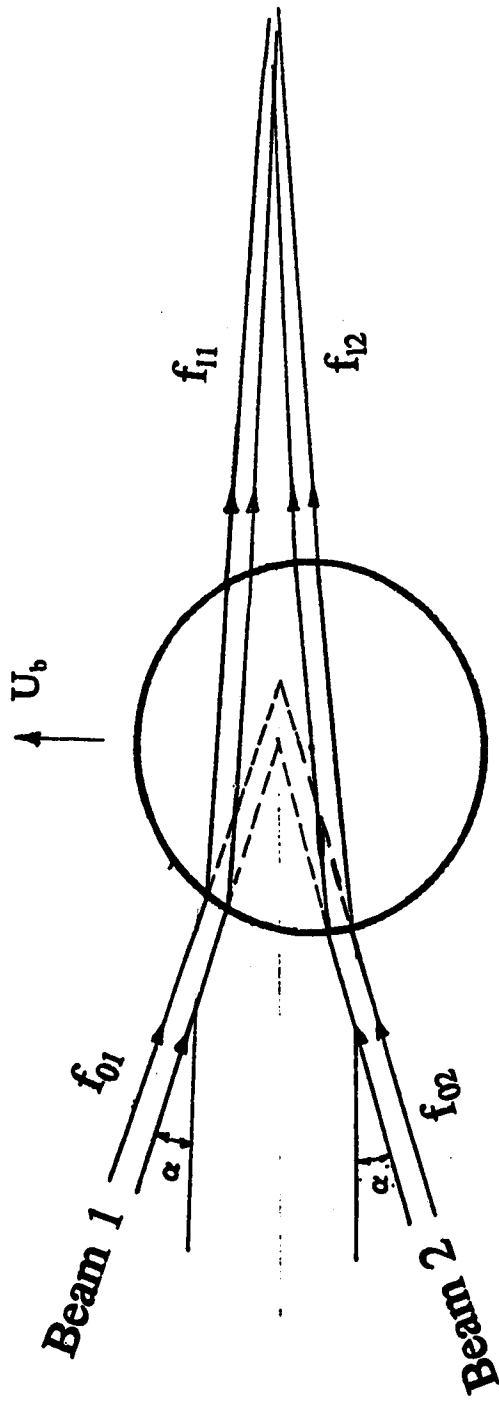


Figure 3.3 The principle of the bubble rising velocity measurement using LDA.

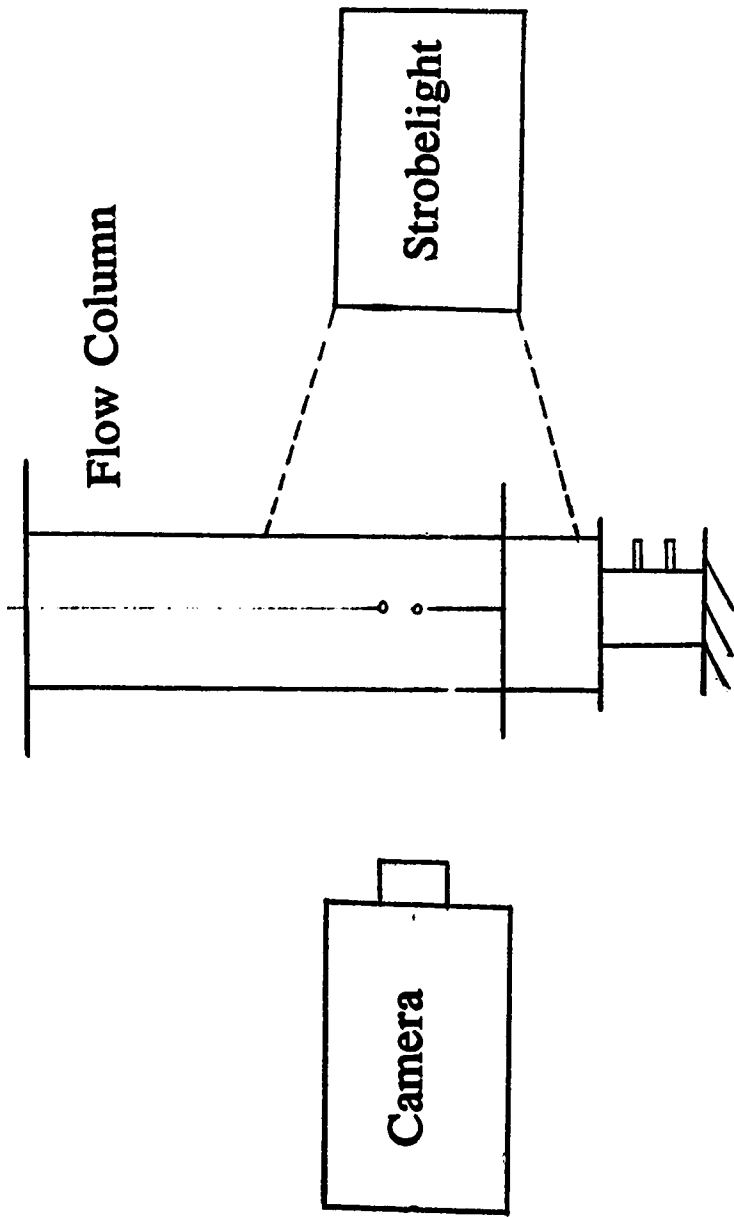


Figure 3.4 Bubble size measurement by photography.

CHAPTER 4 RESULTS AND DISCUSSION

4.1 Variation of Bubble Rising Velocity with Distance above the Nozzle

Figure 4.1 shows the variation of bubble rising velocity with distance above the nozzle (Z_b) for several typical bubble sizes. The equivalent bubble diameter (D_b), which was defined in Section 2.1 (footnote) and will be explained more in Section 4.10., was varied from 0.62 to 1.10 mm. The range of bubble generating frequency (f) was from 0.43 Hz to 1.80 Hz. The air temperature varied from 23°C to 23.7°C. It can be seen from figure 4.1 that the bubble rising velocity increases very rapidly as soon as it leaves the nozzle, and then the acceleration slows down till a maximum velocity is reached. Afterwards, the bubble rising velocity decreases very slowly with distance. It can also be seen that larger bubbles rise faster than smaller bubbles and, smaller bubbles reach their maximum velocities earlier than larger bubbles. The vertical error bars in figure 4.1 indicate the uncertainty of the bubble rising velocity calculated from the correlations for the LDA system in Appendix B.1. The uncertainty of the distance (Z_b) measurement is ± 0.25 mm. It is too small to be shown in figure 4.1. For each bubble size, the first one or two data points which were measured at values of Z_b within a bubble diameter from the nozzle must be interpreted carefully, since in this range of Z_b , bubble rising velocity is multivalued. It is multivalued because the bubble is in the process of detachment at this location.

In figure 4.1, we observed that the bubbles accelerate to a peak velocity and then decelerate slightly. The acceleration of the bubble can be readily understood from the force analysis as discussed in chapter 2: the drag force increases initially with distance until it balances the buoyancy force (at the maximum velocity). The deceleration of the bubble with distance has been discussed by Clift et al. (1978) and Martin and Chandler (1982). These authors attributed the deceleration to the surface active contaminants in the liquid. When the bubbles are first injected into the column, the bubbles are relatively free of surface active contaminants. Gradually the bubble surface will accumulate surface active contaminant which can reduce the internal circulation of bubble and increase the drag. Since the drag force due to the contaminant increases with time, the bubble rising

velocity decreases after a maximum velocity is reached when a force balance is achieved momentarily.

In the present study, only the acceleration phase is considered, and no consideration is given for the effect of surface active contaminants. The maximum velocity will be considered as the terminal velocity, and will be treated as a constant.

4.2 Effects of Bubble Generating Frequency

Figure 4.2 shows the effect of bubble generating frequency on the bubble rising velocity for two representative bubble sizes, 0.67 mm and 1.10 mm in diameter. The bubble rising velocity was measured at a distance of 5.02 mm above the nozzle for $D_e = 0.67$ mm and about 20 mm for $D_e = 1.10$ mm. As can be seen, the bubble rising velocity was not affected significantly by the frequency in the frequency range tested for the two bubbles. The bubble generation frequencies used in the main experiments were all within the range tested for the two bubbles. Thus, it can be assumed that the bubble generation frequency has no effect on bubble rising velocity in the present study.

4.3 Accuracy of Temperature Measurement

In order to facilitate the experiments and also to keep the distilled water in the test section clean, room temperature was measured and was assumed to be the temperature of the water in the test section. In order to justify this assumption, the room temperature and the water temperature just above the tip of the nozzle were measured at the same time for two different days. Figure 4.3 shows the variation of both the room temperature and the water temperature with time for two days from 9 am to 4 pm. The room temperature increased slightly with time whereas the water temperature decreased slightly. However, the maximum temperature difference between the room and the water temperature was 0.7°C. The room temperature and the water temperature were the same at 10 am for the day 1 test, and at 11:30 am for the day 2 test. Most of the experiments in the present study were conducted from 10 am to 12 pm. Therefore, the difference between the room and the water temperature was less than 0.7°C. Figure 4.4 shows the bubble rising velocities at two different room temperatures: 22.8 °C and 24.7 °C. The

room temperature difference was 1.9 °C. We can see from figure 4.4 that the bubble rising velocity is hardly influenced by the temperature difference. Thus, for a smaller temperature difference 0.7° which is the maximum temperature difference between the room temperature and the water temperature, the effect on bubble rising velocity is negligible. Therefore, we can use the room temperature as the water temperature.

4.4 Experiment Repeatability

Two bubbles of different sizes were used to test the repeatability of the experiments. In figure 4.5(a), the experiments were conducted for four runs for a bubble size of 0.67 mm in diameter. In figure 4.5(b), the experiments were conducted twice for a bubble size of 1.10 mm in diameter. In all cases, the experiments had good repeatability.

4.5 Terminal Velocity (Maximum Velocity)

Wallis (1974) reviewed the terminal velocity for both fluid spheres and solid spheres and arrived at two equations. These two equations are shown in figure 4.6 as two straight lines. Figure 4.6 shows the dimensionless terminal velocity versus the dimensionless radius. The upper bound straight solid line corresponds to fluid spheres and the lower bound straight dash line corresponds to solid spheres. The dimensionless variables are defined as:

$$V^* = V \left(\frac{\rho^2}{\mu g \Delta \rho} \right)^{\frac{1}{3}}$$

$$R^* = R \left(\frac{\rho g \Delta \rho}{\mu^2} \right)^{\frac{1}{3}},$$

where: V (U_{bT} in present study) is the dimensional velocity, ρ is the liquid density, $\Delta \rho$ is the density difference between the two phases, μ is the viscosity of the liquid and R ($D_c/2$ in present study) is the dimensional radius.

Two sets of experimental results are shown in figure 4.6. One set is from the

present experiments where the dimensionless velocity was calculated based on the maximum velocity. The other data set reports the results from Martin and Chandler (1982). We can see that all the experimental results are close to the upper bound straight solid line for fluid spheres. This supports the conclusion that the air bubble behaves more like a fluid sphere than a solid sphere. The present dimensionless maximum velocities are also close to Martin's data.

4.6 Theoretical Prediction

As mentioned in Chapter 2, in order to solve the governing equation (equation 2.2.5) to predict the bubble rising velocity, the drag force must be determined first. The drag force includes the quasi-steady term, the added-mass term and the history term. The history term was neglected because it is usually assumed to be unimportant compared with the other two terms according to the literature (Kuo and Wallis, 1988). Thus, only the quasi-steady term and the added-mass term were considered. For the quasi-steady term, four drag coefficients, which were $C_D = 14.9 \text{ Re}^{-0.78}$ (numerical solution), $C_D = 13.73 \text{ Re}^{-0.74}$ (the error distribution solution), $C_D = 48/\text{Re}$ (Levich boundary layer solution) and $C_D = 48/\text{Re} [1 - 2.21/\text{Re}^{1/2} + o(\text{Re}^{-5/6})]$ (Moore boundary layer solution) discussed in Chapter 2, were used. As for the added-mass coefficient, a value of 1.0 was used in solving the governing equation to predict the experimental results. This value is for unsteady creeping flow (Clift et al., 1978) and has been used for high Reynolds number bubble acceleration (Varty, 1991a). Other values for the added-mass coefficient were also used and the predicted results will be discussed in Section 4.8.

The governing equation (ODE) was solved numerically by using the fourth-order Runge-Kutta method. The distance Z_b was integrated from the numerical values of U_b and t by using the Simpson's 1/3 Rule. The maximum error of the numerical values of Z_b obtained by using these two methods is 0.000012%.

Figure 4.7 shows the comparison of the bubble rising velocities (versus the distance) between the experimental results and the theoretical predictions for four bubble sizes. It can be seen that for any bubble size, the difference between the predictions (lines) using different C_D formulae is very small in the initial stage of bubble rising. All

the theoretical lines fit the experimental data well, especially for large bubbles. As the maximum velocity is approached, some of the theoretical lines start to deviate from the experimental data. A close examination of all the plots for different bubble sizes reveals that the theoretical line using $C_D = 14.9\text{Re}^{-0.78}$ gives the best prediction of the bubble rising velocity.

It is to be noted that the drag force coefficient $C_D = 14.9\text{Re}^{-0.78}$ is from the numerical solution of the Navier-Stokes equation (for steady flow). Therefore, what we observe in figure 4.7 is consistent with the conclusion that numerical solution for the evaluation of C_D gives the most complete and reliable results (Clift et al. 1978).

It can be recalled from Chapter 2 that the analytic solution using the drag coefficient $C_D = 48/\text{Re}$ gives a good prediction for a bubble size 1 mm in diameter (Varty, 1991a). The theoretical lines using this drag coefficient in figure 4.7 give lower predictions for bubble sizes less than 1 mm in diameter and gives a higher prediction for a bubble size larger than 1 mm. Therefore, the present data support Varty's conclusion.

4.7 Evaluation of a New C_D Form from the Present Experiments

In the above section, all the C_D forms used are from theoretical solutions. Alternatively, one can evaluate the drag coefficient based on the maximum or terminal velocity, and then use the experimentally determined C_D to predict the bubble rising velocity during acceleration.

At steady state where the maximum or terminal velocity is reached, a force balance between the buoyancy force and the drag force gives:

$$C_D = \frac{4 D_b g \Delta \rho}{3 \rho U_{bT}^2}, \quad (4.7.1)$$

where: U_{bT} is the maximum bubble rising velocity and D_b is a spherical bubble diameter. In the present study, the larger bubbles have ellipsoidal shapes. The maximum aspect ratio is 1:1.16 which is close to a spherical shape. Therefore, the bubbles were treated as spherical bubbles with the volume-equivalent bubble diameter (D_e)(see Section 4.10).

The C_D was calculated from the above equation using the volume-equivalent bubble diameter.

Figure 4.8 shows the plot of C_D versus the Reynolds number based on the maximum bubble rising velocity. A regression of the data using least square analysis gives:

$$C_D = 11.91Re^{-0.74} . \quad (4.7.2)$$

Figure 4.9 shows the comparison between the experimental data and the predictions for the bubble rising velocity using the new C_D form (equation 4.7.2). It is evident that the new C_D form gives good predictions for the bubble rising velocity for all bubble sizes. Also shown in figure 4.9 is the theoretical predictions using $C_D = 14.9Re^{-0.78}$. As expected, the theoretical prediction using the new C_D form works slightly better than $C_D = 14.9 Re^{-0.78}$, particularly for the two smaller bubbles.

4.8 Discussion of the Added-Mass Coefficient

In order to find how the value of the added-mass coefficient influences the prediction, several different values for Δ_A are used. The solutions are shown in figure 4.10 again for the four bubble sizes. The new drag coefficient form (equation 4.7.2) is used and three different values for the added-mass coefficient, namely, 0.5, 1.0 and 2.0 are used. It can be seen that the most obvious difference in the predictions are in the corner of the curves where the maximum velocity is approached. The lower value (0.5) for the added-mass coefficient gives higher predicted values for the bubble rising velocity. This is expected due to the fact that a lower value for Δ_A means a smaller drag force. Figure 4.10 shows that a value of 1.0 gives the best prediction for the bubble acceleration. Although this value is originally for unsteady creeping flow, apparently it can also be used for unsteady higher Reynolds number flow. It should be noted that potential flow around a sphere, $\Delta_A = 1.0$ is the exact value.

4.9 Variation of the Quasi-Steady Drag Force and the Added-Mass Force with Distance

Figure 4.11 shows the variation of the quasi-steady drag force and the added-mass force with the distance. The quasi-steady force was calculated from equation 2.2.7 and the added-mass force was calculated from equation 2.2.8. In the calculations of F_{Ds} , the new form of C_D (equation 4.7.2) was used. The quasi-steady drag force increases very rapidly with the distance initially and then levels off when the maximum velocity is reached. This is because the quasi-steady drag force is proportional to $U_b^{1.26}$.

Contrary to the quasi-steady drag force, the added-mass force decreases sharply with the distance initially and then gradually reaches zero when the maximum velocity is reached where the bubble acceleration is zero. The difference between the added-mass forces using different values of Δ_A and the difference between the quasi-steady drag force using different values of Δ_A are more pronounced in the distance range of approximately 3 to 10 mm. The lower the added-mass coefficient, the lower the added-mass force. Whereas the lower the added-mass coefficient, the higher the quasi-steady drag force. This is because low added-mass force (or low added-mass coefficient) causes high bubble rising velocity and the quasi-steady drag force is proportional to $U_b^{1.26}$.

The total drag force ($F_{Ds} + F_{DA}$) varying with distance is shown in figure 4.12. The main difference between total drag forces obtained by using different values of the added-mass coefficients occurs in the initial distance range of 0 to 10 mm. The curve for the total drag force obtained by using the added-mass coefficient 0.5 is named curve 0.5. Similarly, the other two curves are named curve 1 and curve 2. From this plot, curve 0.5 is below curve 1 before the distance of 3 mm. After this distance, curve 0.5 is above curve 2. Since a lower drag causes a higher bubble acceleration, whereas a higher drag causes a lower bubble acceleration, the bubble acceleration is higher by using $\Delta_A=0.5$ than using $\Delta_A=1$, and the difference between the bubble rising velocities obtained by using these two added-mass coefficients increases with the distance until it reaches the distance of 3 mm (figure 4.10(d)). After this distance the bubble acceleration becomes lower by using $\Delta_A=0.5$ than using $\Delta_A=1$, and the difference between the bubble rising velocities obtained by using these two added-mass coefficients decreases with the distance. Eventually the bubble accelerations for both cases are zero and the difference between the bubble rising velocities obtained by using the two values is zero.

The crossing point at the distance 3 mm is a critical point where the maximum difference of bubble rising velocities for two different added-mass coefficients 0.5 and 1 occurs. This distance will be different for other bubble sizes. Similarly, at the distance of 3.7 mm, the maximum difference between the bubble rising velocities obtained by using $\Delta_A=0.5$ and 2 occurs. At 5.5 mm, the maximum difference between the bubble rising velocities obtained by using $\Delta_A=1$ and 2 occurs. These three critical points are shown in the distance range of 3 to 6 mm in figure 4.12. The corresponding maximum velocity differences for the same size bubble can be found in figure 4.10 (d) at the same 3 critical points.

4.10 Discussion on Bubble Shape

In all the calculations discussed above, we have assumed that the bubbles are spherical and an equivalent bubble diameter has been used. The deviation of the bubble shape from spherical is due to the bubble motion which increases the pressure gradients surrounding the bubble. The pressure distribution becomes less uniform on the bubble surface and consequently, the bubble deforms from spherical to ellipsoidal.

The equivalent bubble diameter is calculated as follows. Both the long and the short axes (D_y and D_z , where D_y is the horizontal dimension and D_z is the vertical dimension) are measured from the photographs and the volume of the ellipsoid is calculated from equation $V = \pi/6 D_z D_y^2$. Thus, the equivalent bubble diameter can be determined based on the same volume from the equation $D_e = (6V/\pi)^{1/3}$.

Figure 4.13 shows the variation of the bubble aspect ratio (D_z/D_y) with distance for a bubble of 1.10 mm in diameter. The aspect ratio decreases with increasing distance. The variation of the equivalent bubble diameter with distance for this bubble is shown in figure 4.14. Although the aspect ratio decreases by about 15% within the distance measured, the equivalent bubble diameter changes very little with the distance. In all the calculations discussed in previous sections, an average value for the equivalent bubble diameter is used.

4.11 Non-Dimensional Representation of the Data and Correlations

It would be desirable to correlate all the data for different bubble sizes and arrive at a unique correlation. An effort was thus made to search for suitable non-dimensional groups. The details are given in Appendix C. The two non-dimensional groups found are:

$$U^* = \frac{U_b}{U_{bT}} , \quad Z^* = \frac{(z_b - z_{bo})g}{U_{bT}^2} \approx \frac{z_b - z_{bo}}{D_c} \frac{1}{Fr}$$

Figure 4.15 shows the correlation between the two non-dimensional groups. It can be seen that there is a very good correlation between the dimensionless bubble rising velocity and the dimensionless distance for nine different bubble sizes³ tested.

The variation of the dimensionless bubble rising velocity with the dimensionless distance can be predicted from the new C_D form evaluated from the present study based on the maximum velocity. This can be done for any bubble size. Figure 4.15 shows such a prediction for a bubble size of $D_c = 1.10$ mm as the solid line.

³The experiments were conducted for five different bubble sizes without measuring the air temperature. Therefore they were not used for the theoretical predictions in previous sections. They are used here because temperature does not need to be known to form the two dimensionless groups plotted here. The five volume-equivalent bubble diameters are 0.59, 0.65, 1.03, 1.12 and 1.23 mm.

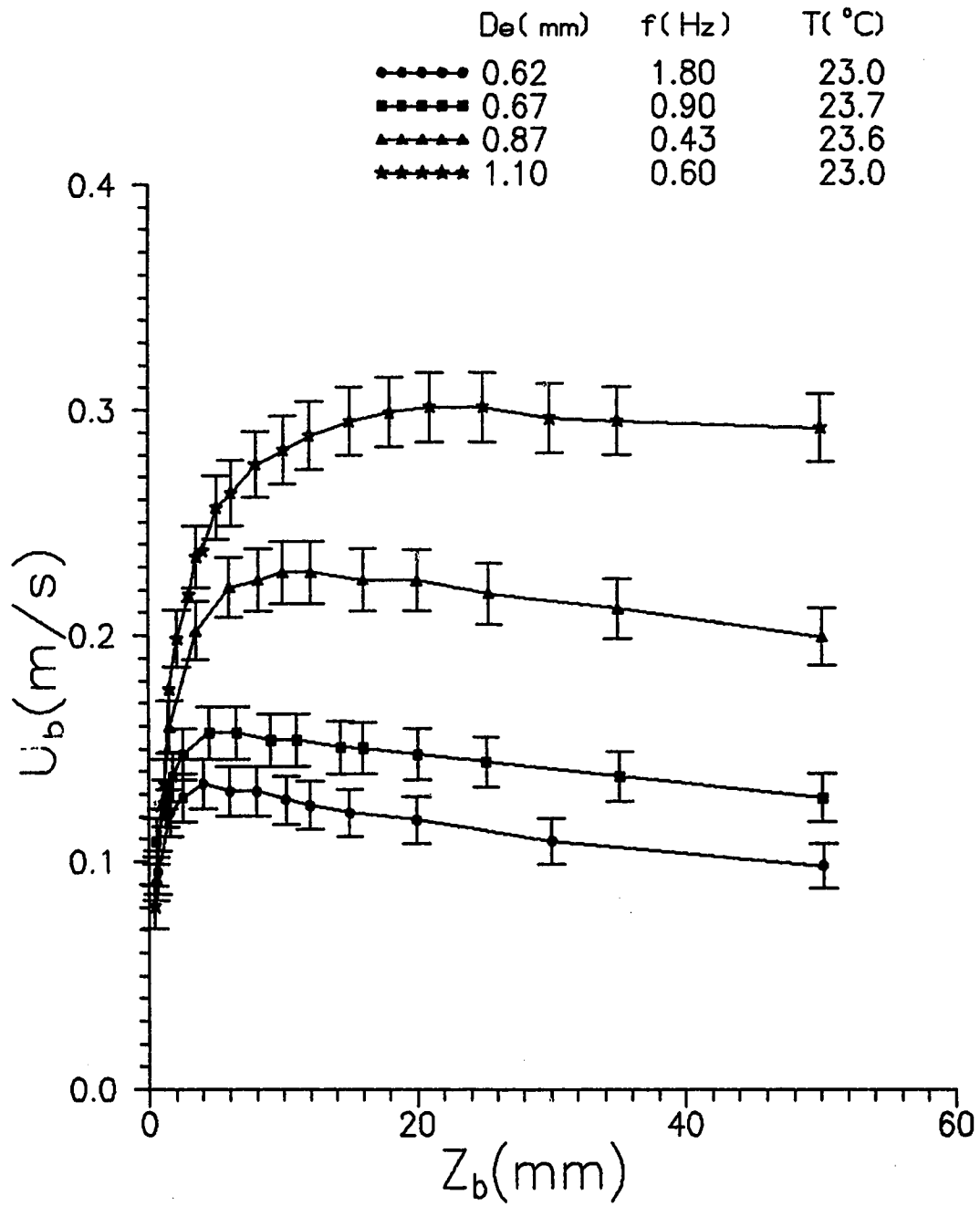


Figure 4.1 Variation of bubble rising velocity with distance above the nozzle for different bubble sizes.

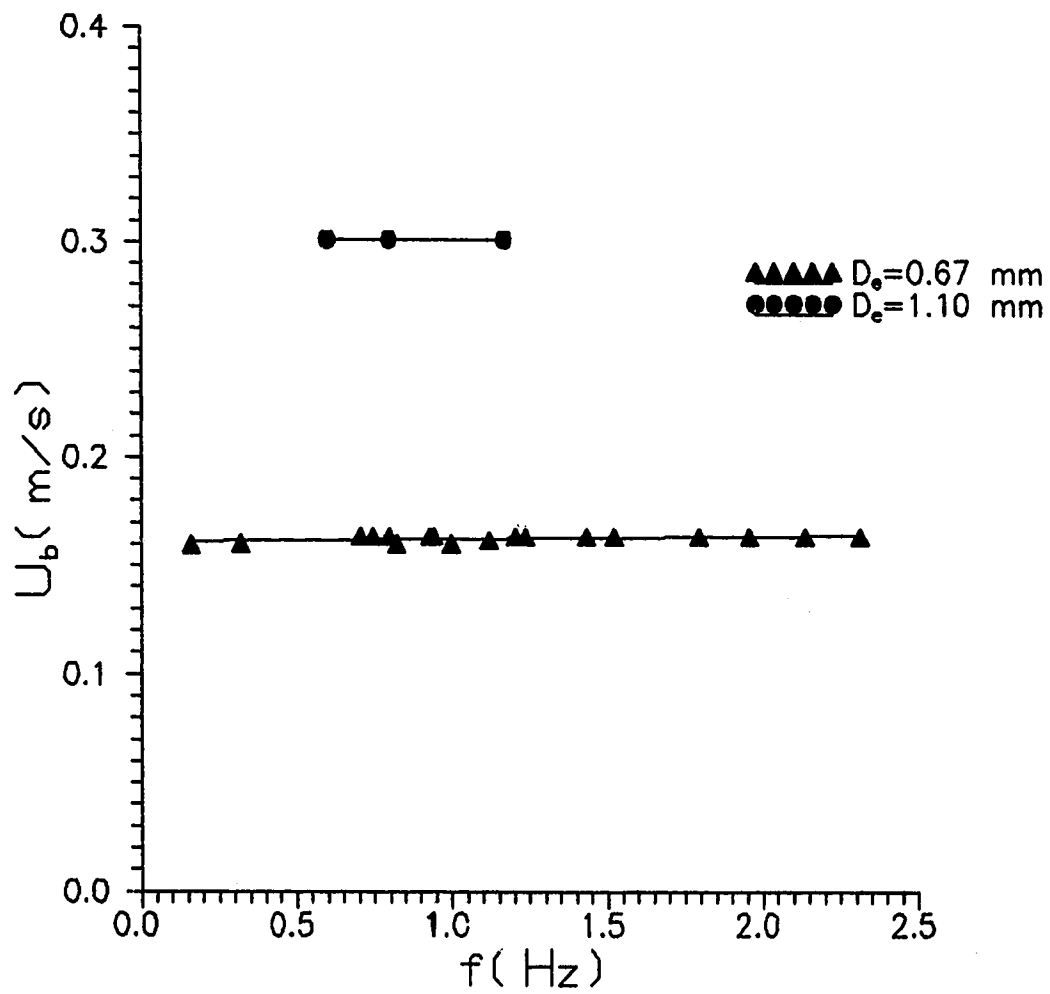


Figure 4.2 Effect of bubble generating frequency on bubble rising velocity for two different bubble sizes.

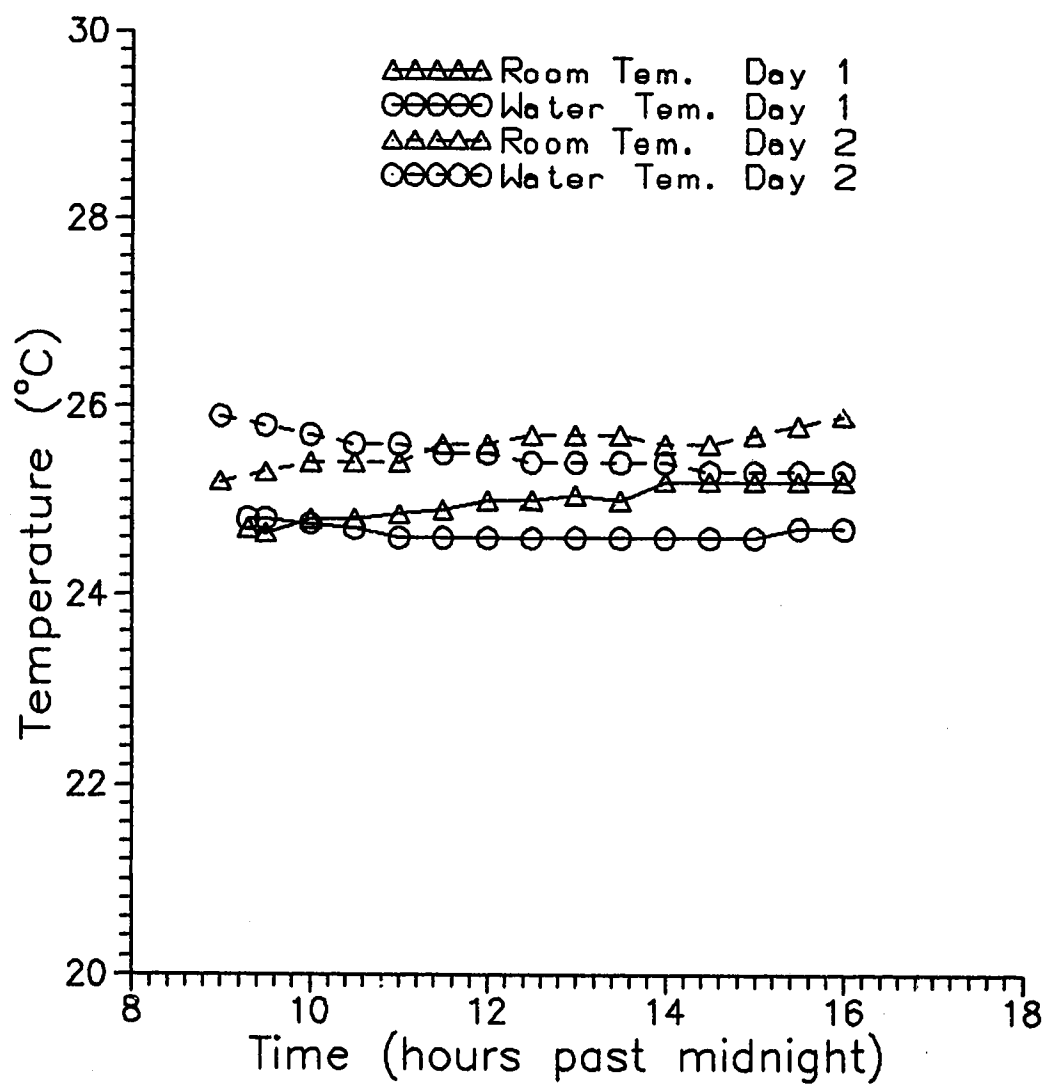


Figure 4.3 Variation of room temperature and water temperature with time.

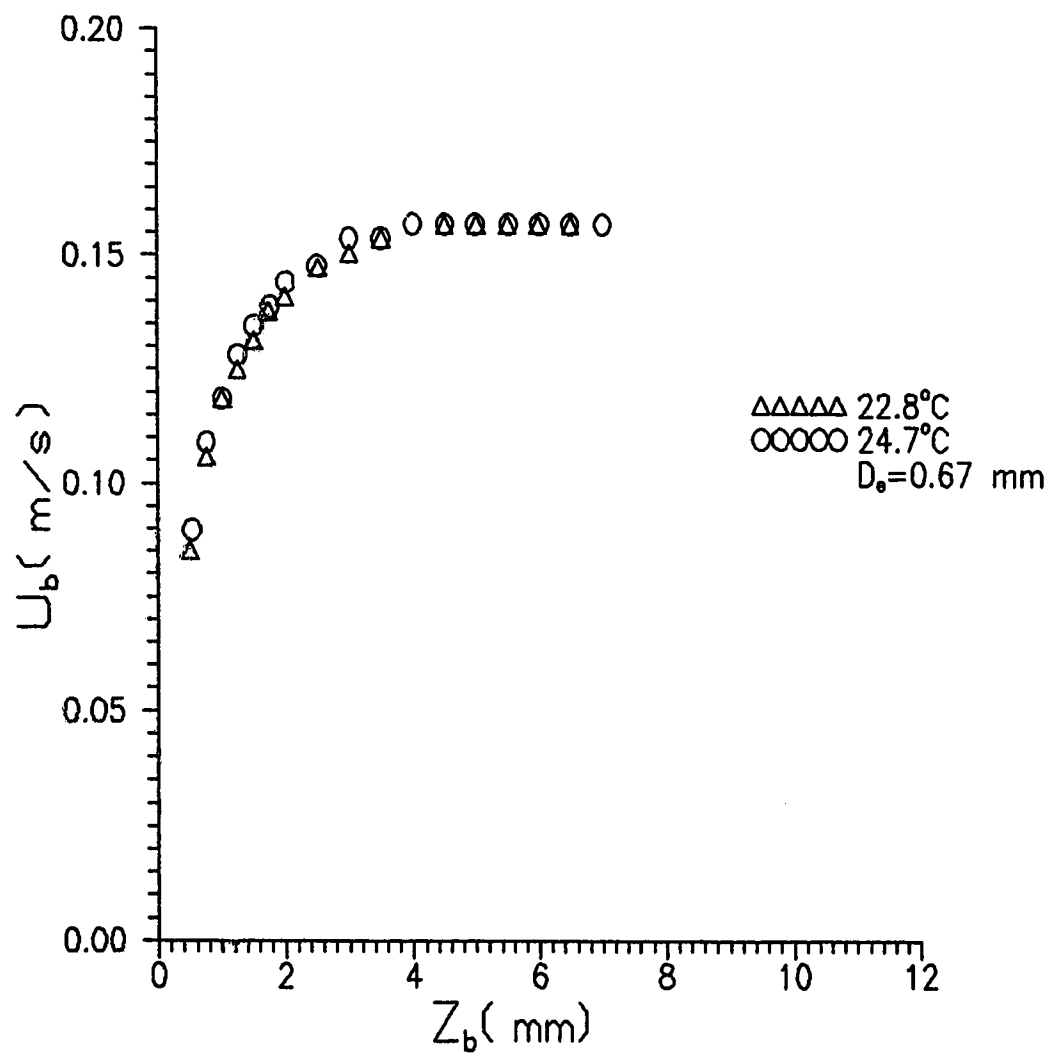


Figure 4.4 Effect of temperature variation on bubble rising velocity.

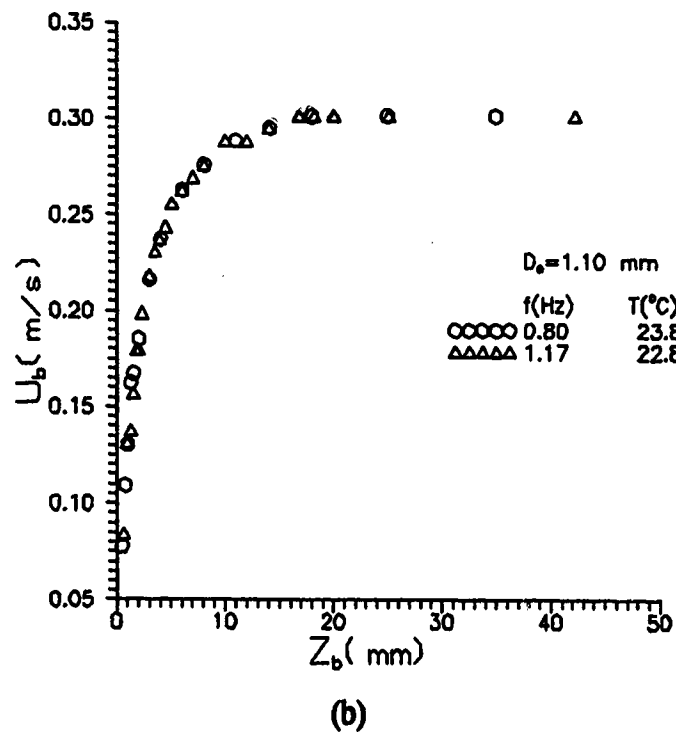
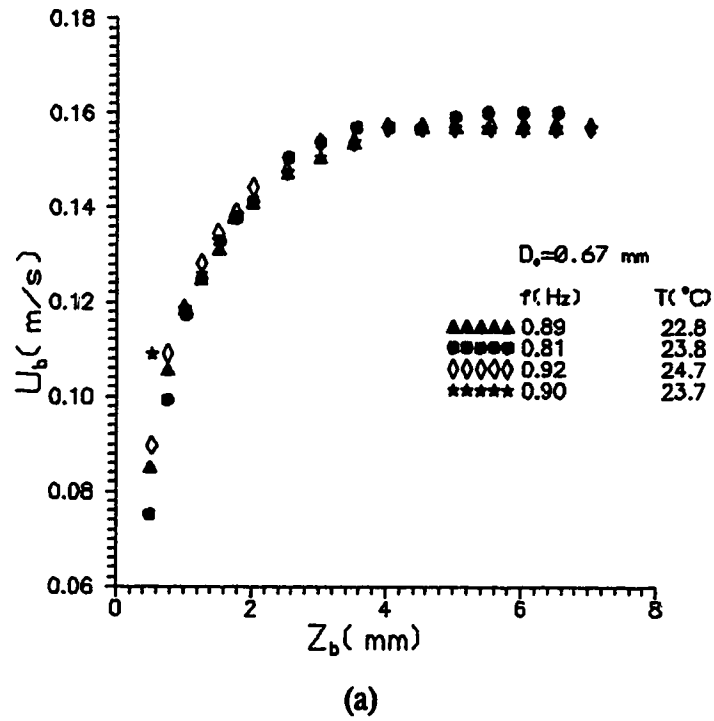


Figure 4.5 Test of experiment repeatability, (a) $D_e = 0.67$ mm, (b) $D_e = 1.10$ mm.

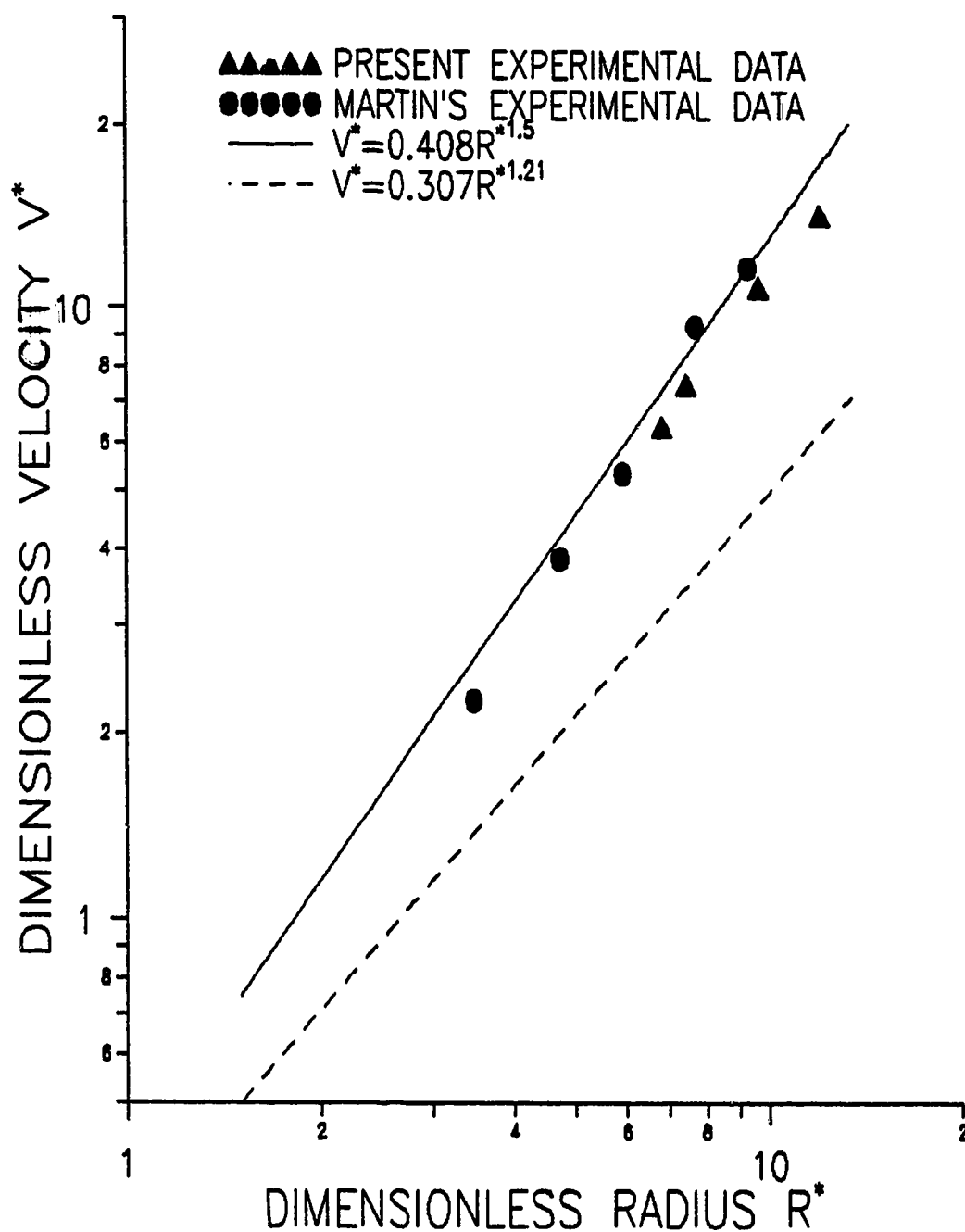


Figure 4.6 Comparison of the maximum bubble rising velocity between the present study and the literature results.

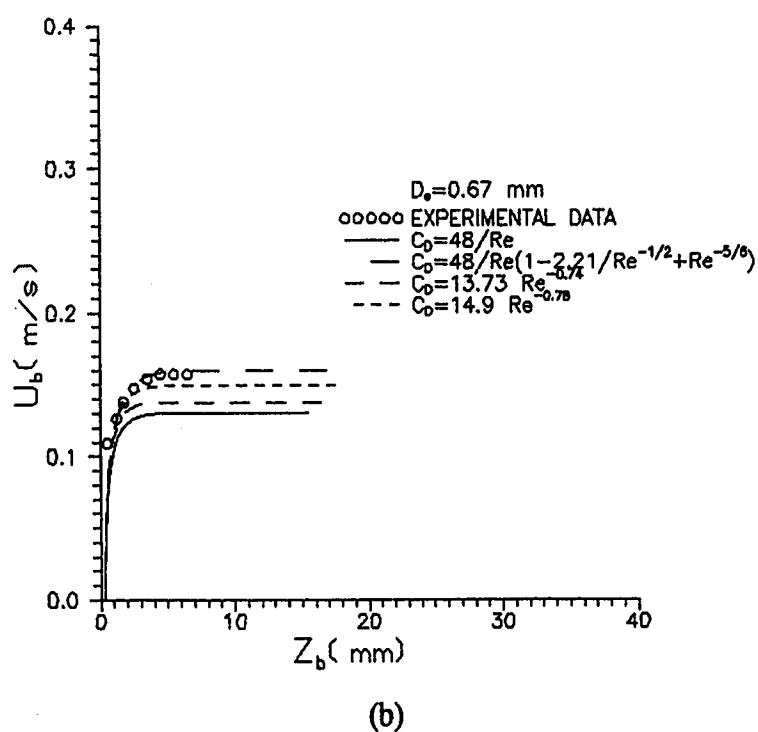
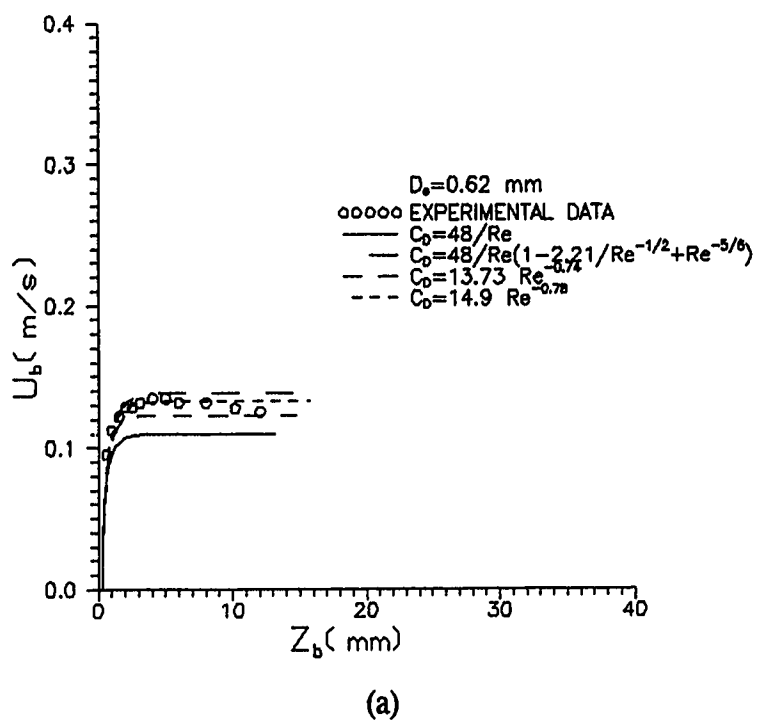


Figure 4.7 Prediction of the bubble rising velocity using different C_D forms at $\Delta_A = 1.0$.

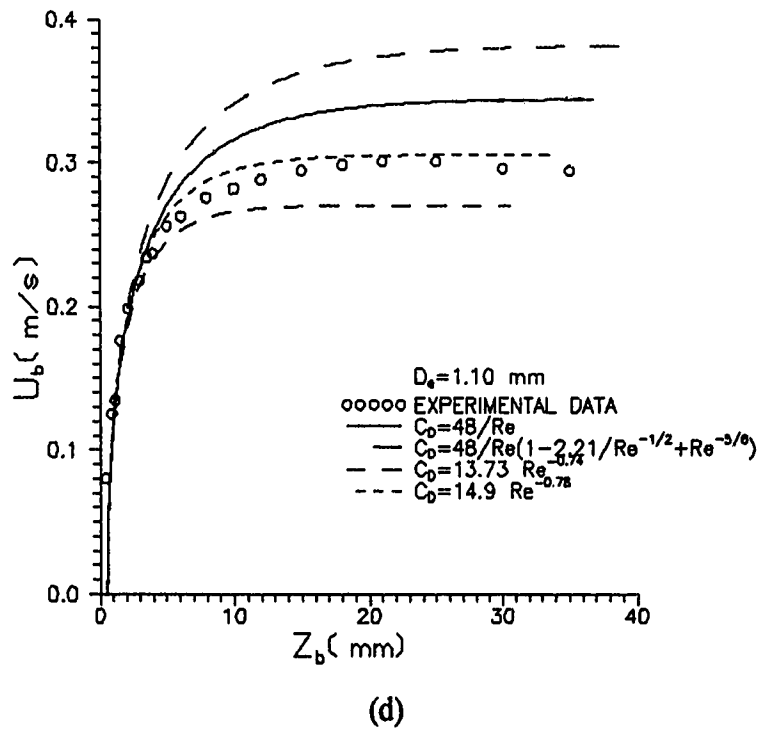
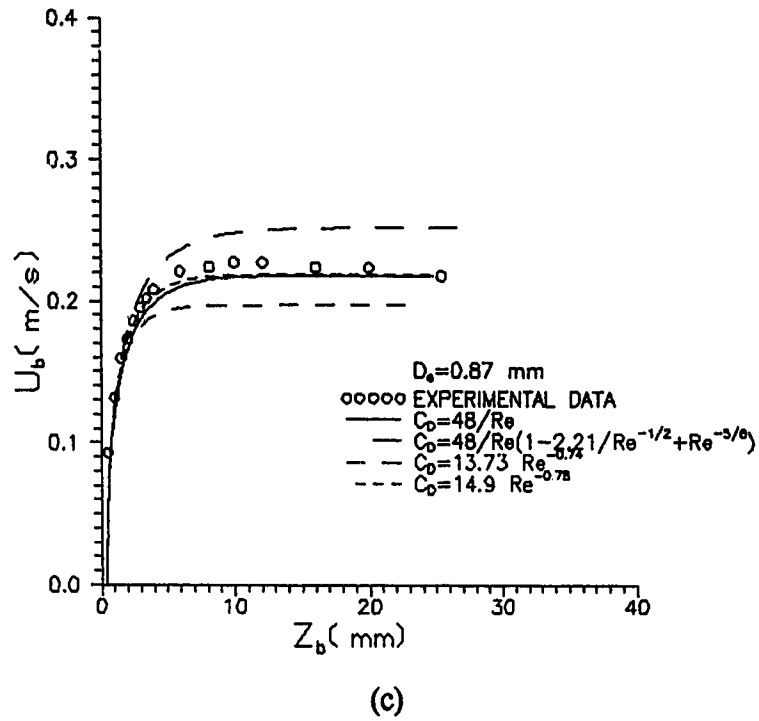


Figure 4.7 Prediction of the bubble rising velocity using different C_D forms at $\Delta_A = 1.0$.

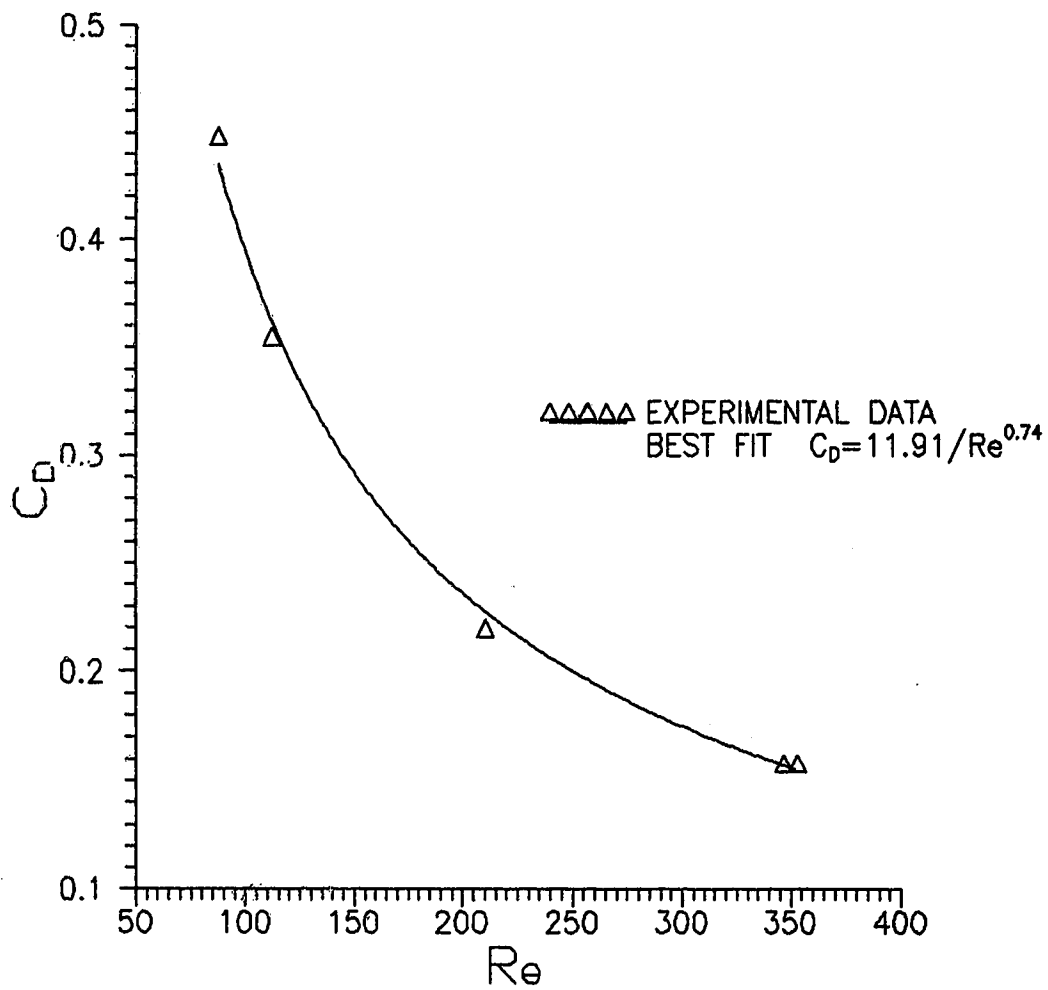


Figure 4.8 Evaluation of the steady drag coefficient based on the maximum bubble rising velocity.

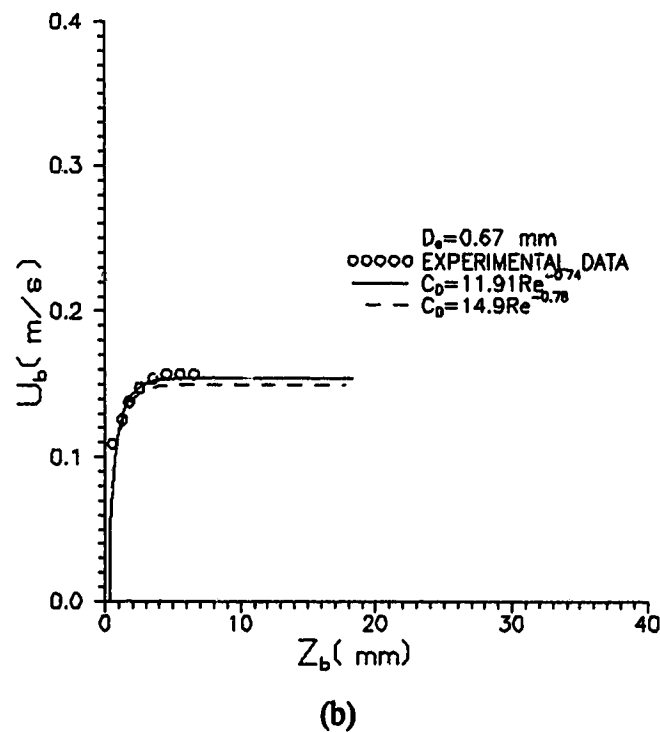
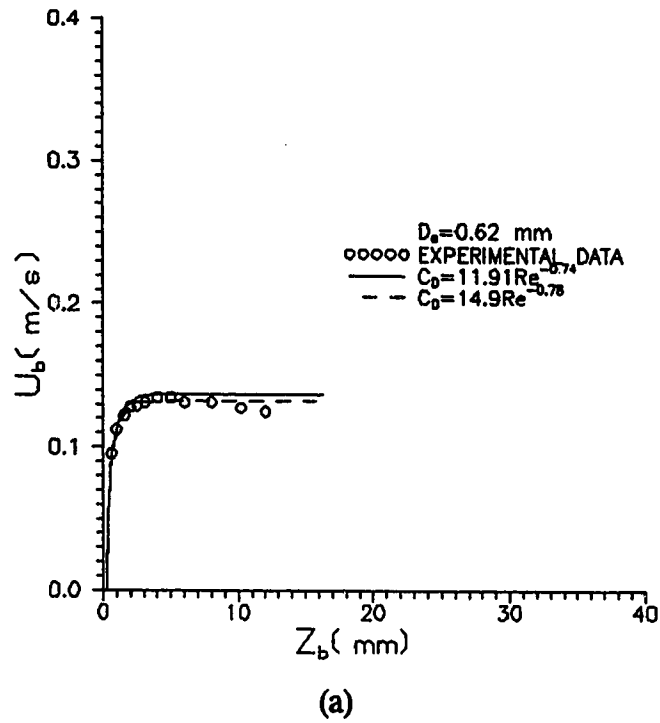


Figure 4.9 Comparison between the experimental data and the predictions for the bubble rising velocity using the new C_D at $\Delta_A = 1.0$.

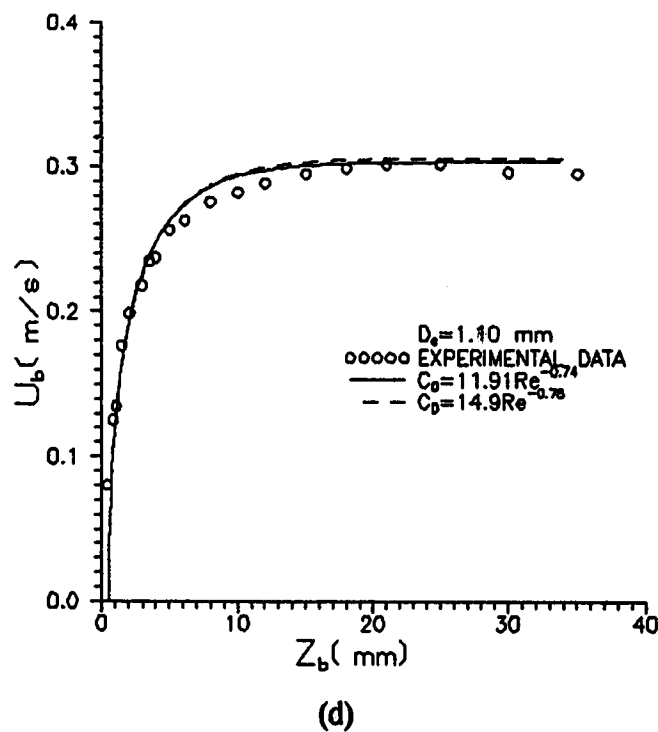
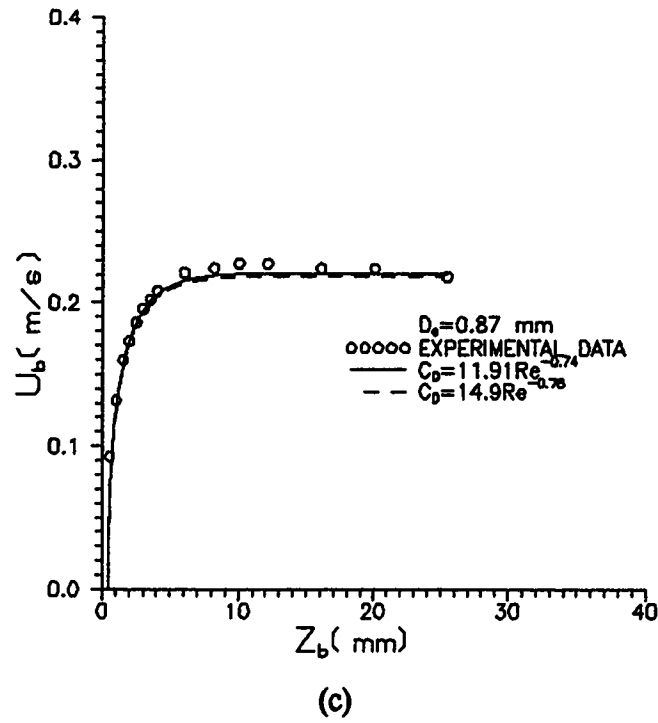
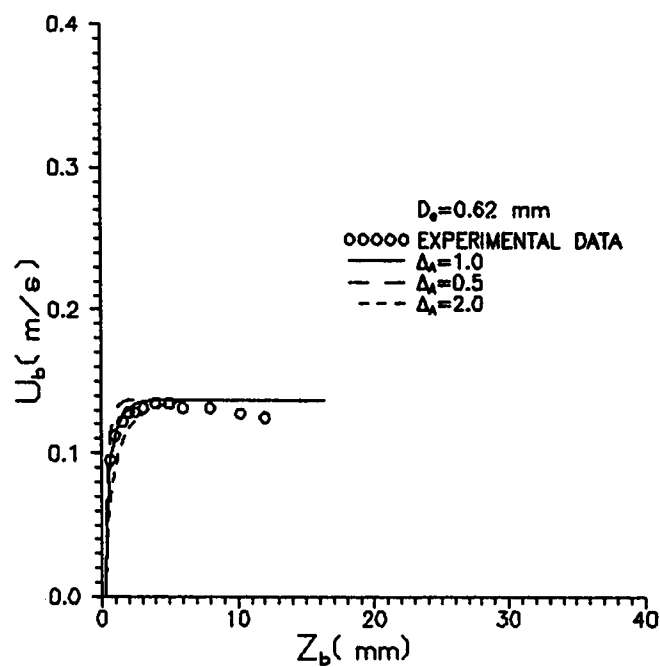
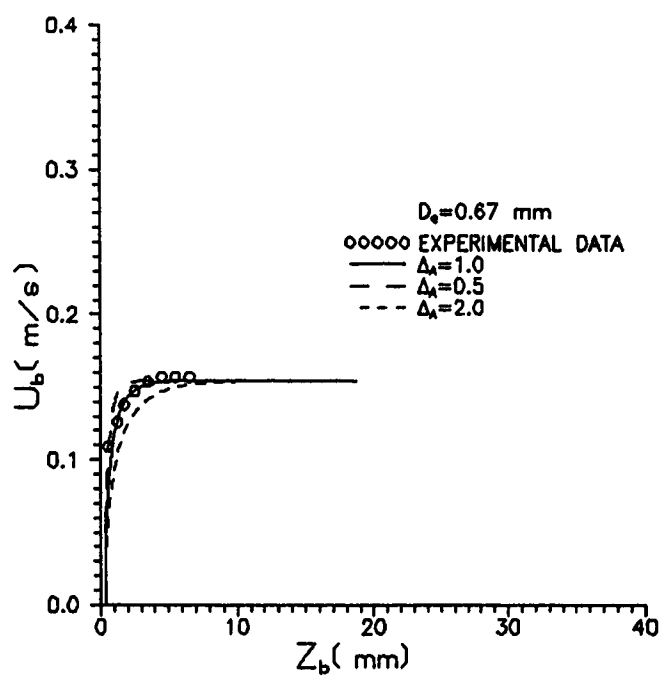


Figure 4.9 Comparison between the experimental data and the predictions for the bubble rising velocity using the new C_D at $\Delta_A = 1.0$.



(a)



(b)

Figure 4.10 Effect of the added-mass coefficient at different values on the prediction of bubble rising velocity

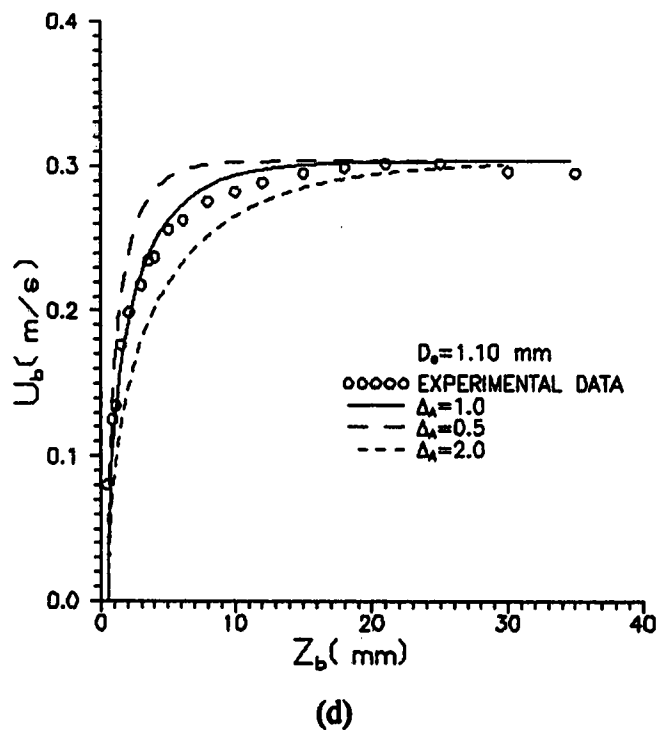
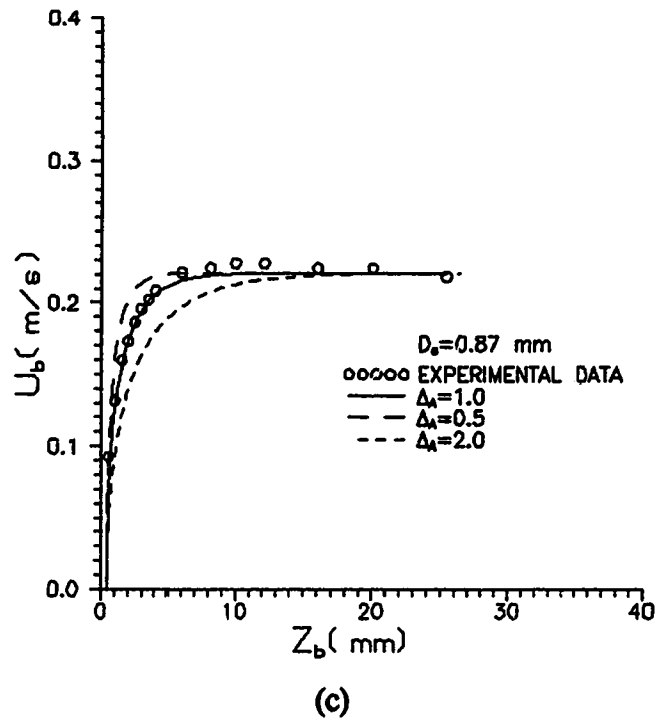


Figure 4.10 Effect of the added-mass coefficient at different values on the prediction of bubble rising velocity

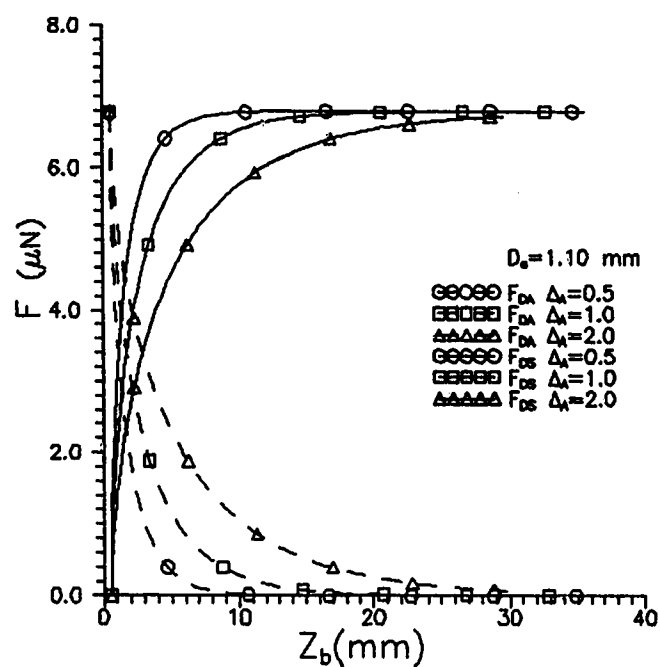


Figure 4.11 Variation of the quasi-steady drag force and the added-mass force with distance.

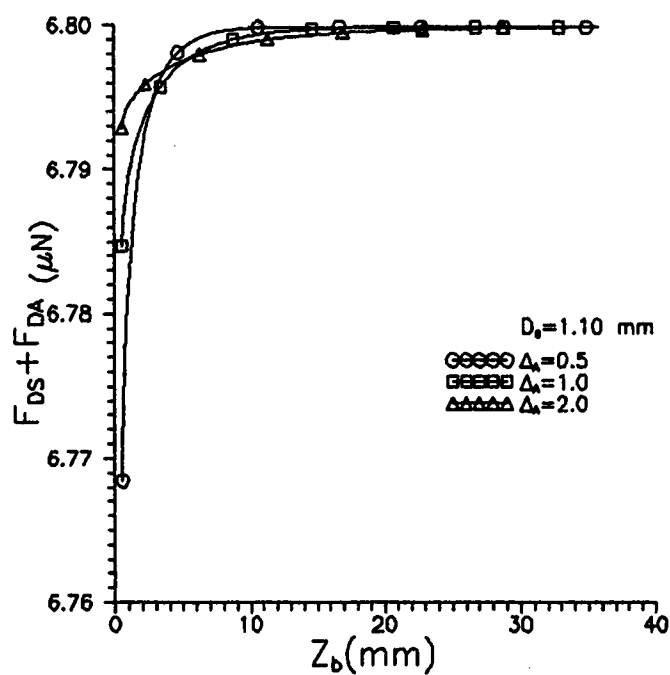


Figure 4.12 Variation of total drag force with distance.

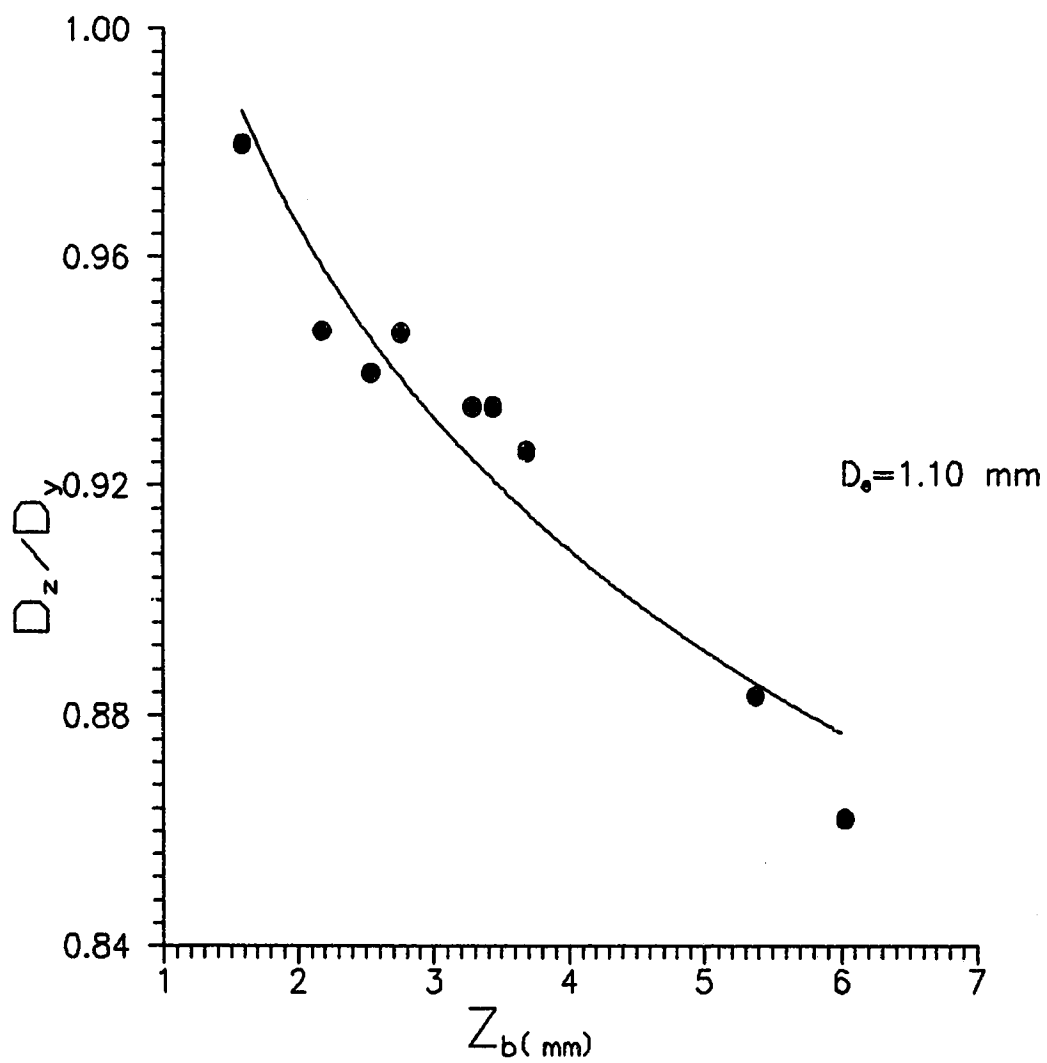


Figure 4.13 Variation of the bubble aspect ratio with distance.

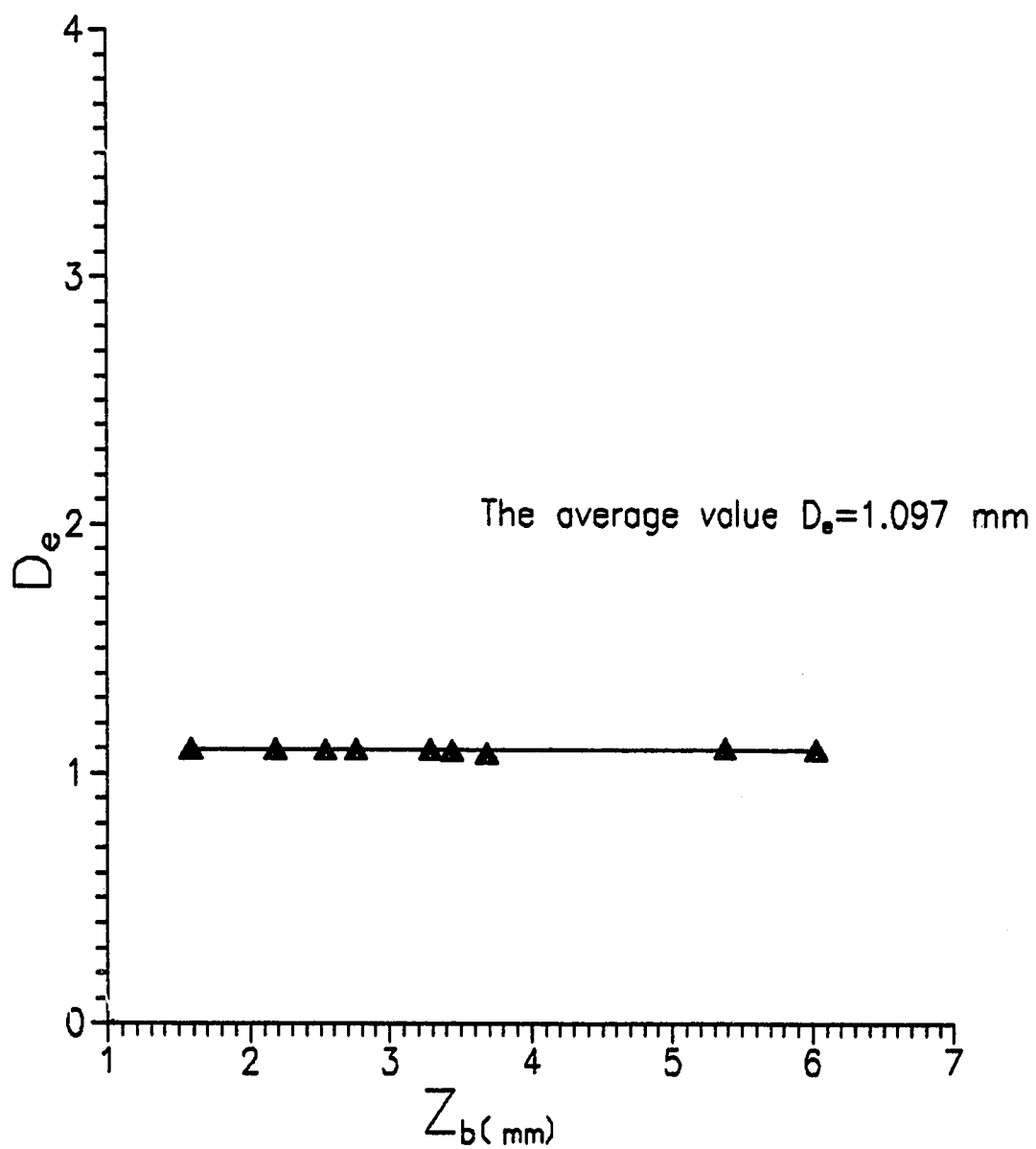


Figure 4.14 Variation of the volume-equivalent bubble diameter with distance.

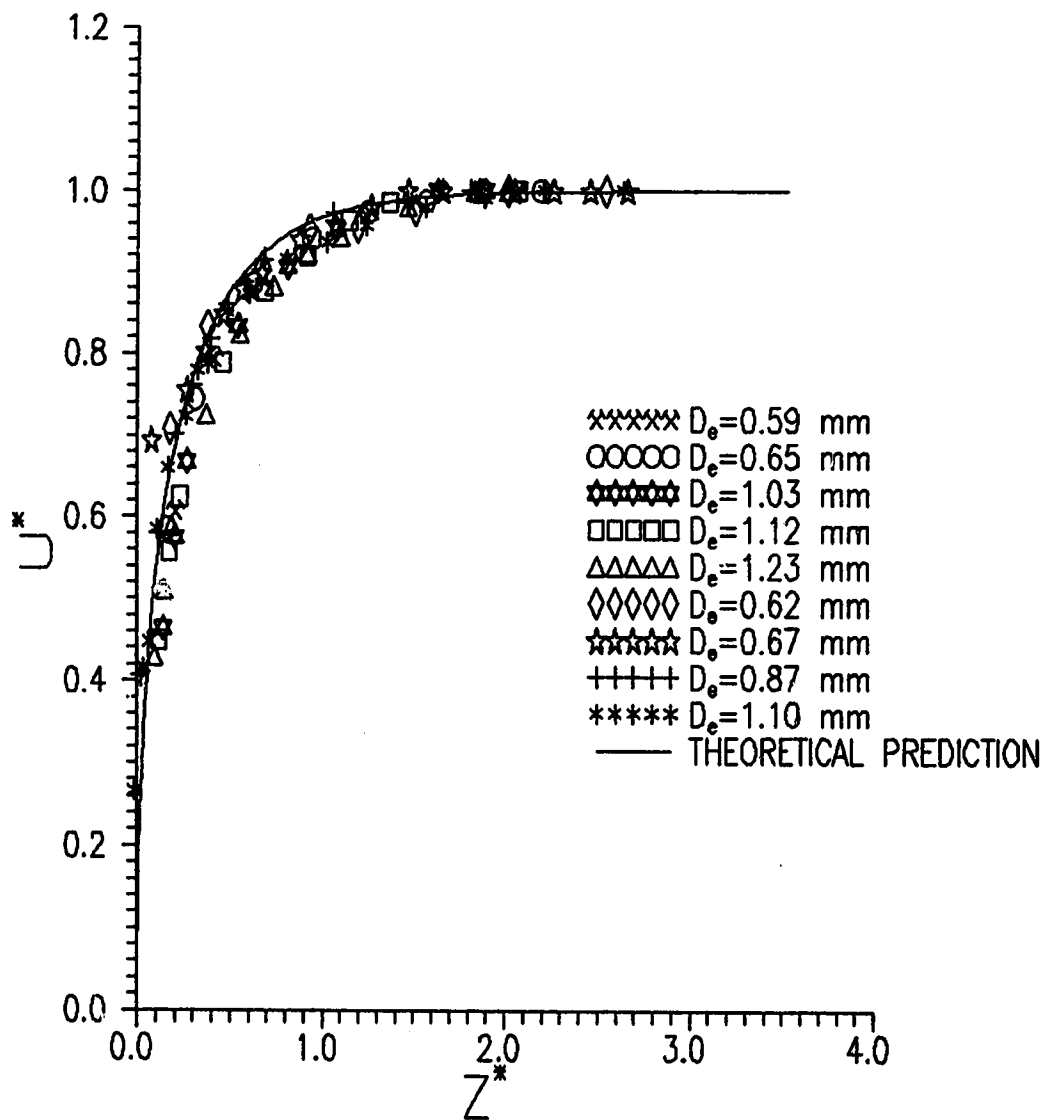


Figure 4.15 Variation of the dimensionless velocity with the dimensionless distance.

CHAPTER 5 CONCLUSIONS

The objectives of this study were to measure bubble rising velocity and to find a suitable mathematical model to predict the bubble acceleration at Reynolds numbers for 0 to 400.

The bubble shape within the size range studied was essentially spherical, and rectilinear motion was observed. The bubble rising velocity can be measured very accurately using LDA. It was observed that the bubble accelerated to a maximum velocity and then decelerated very slowly with the distance travelled. Smaller bubbles reached their maximum velocities earlier than larger bubbles. The bubble generating frequency around one Hz had a negligible effect on bubble rising velocity.

Several correlations or equations from the literature for the quasi-steady drag coefficient were used in solving the governing equations to predict the bubble acceleration. It was found that all the drag coefficients from the literature gave good predictions for the bubble rising velocity in the initial acceleration. It was possible to use the previously calculated drag coefficient $C_D = 14.9\text{Re}^{-0.78}$ to predict the bubble rising velocity throughout the whole acceleration period for all the bubble sizes tested.

A new correlation for the (quasi-steady) drag coefficient, $C_D = 11.91 \text{Re}^{-0.74}$, was obtained from the present study. The drag coefficient was evaluated based on a force balance on the bubble at the maximum velocity. The use of this new drag coefficient gave a slightly better prediction than $C_D = 14.9\text{Re}^{-0.78}$ for the bubble rising velocity.

Different values for the added mass coefficient were used in solving the governing equation. A value of 1.0 gave the best prediction for the bubble rising velocity for all sizes of bubbles. This can be expected, because it is the value for unsteady creeping flow.

Using the dimensionless variables developed in the present study, a unique correlation was obtained between the bubble rising velocity and the distance for all the bubble sizes studied. It collapsed the data for several different bubble sizes quite well.

REFERENCES

- Basset, A. B., 1961(Republished), *A Treatise on Hydrodynamics*, Vol. 2, Dover, New York. (First Published 1888, Deighton Bell, Cambridge, England.)
- Blanchard, D. C., and Syzdek, L. D., 1977, "Production of Air Bubbles of a Specified Size," *Chem. Engng. Sci.*, Vol. 32, pp. 1109-1112.
- Brabston, D. C., and Keller, H. B., 1975, "Viscous Flows Past Spherical Gas Bubbles," *J. Fluid Mech.*, Vol. 69, pp. 179-189.
- Clift, R., Grace, J. R., and Weber, M. E., 1978, *Bubbles, Drops and Particles*, Academic Press, New York.
- Durst, F., and Zaré, M., 1975, "Laser Doppler Measurements in Two-Phase Flows," *Universität Karlsruhe Report SFB 80/TM/63*.
- Durst, F., 1978, "Studies of Particle Motion by Laser Doppler Techniques," *Proc. Dynamic Flow Conference*, Marseille and Baltimore, pp. 345-372.
- Durst, F., 1982, "Combined Measurements of Particle Velocities, Size Distributions and Concentrations," *Trans. ASME, J. Fluid. Engng*, Vol. 104, pp. 284-296.
- Haas, U., Schmidt-Traub, H., and Brauer, H., 1972, "Umströmung Kugelförmiger Blasen mit innerer Zirkulation," *Chem.-Ing.-Tech.*, Vol. 44, pp. 1060-1068.
- Hadamard, J. S., 1911, *C. R. Acad. Sci.*, Vol. 152, pp. 1735-1738.
- Hamielec, A. E., and Johnson, A. I., 1962, "Viscous Flow Around Fluid Spheres at Intermediate Reynolds Numbers," *Can. J. Chem. Eng.*, Vol. 40, pp. 41-45.
- Hamielec, A. E., Storey, S. H., and Whitehead, J. H., 1963, "Viscous Flow Around Fluid Spheres at Intermediate Reynolds Numbers (II)," *Can. J. Chem. Eng.*, Vol. 41, pp. 246-251.
- Hamielec, A. E., Johnson, A. I., and Houghton, W. T., 1967, "Viscous Flow Around Circulating Spheres of Low Viscosity," *AIChE J.*, Vol. 13, pp. 220-224.
- Kuo, J. T., and Wallis, G. B., 1988, "Flow of Bubbles through Nozzles," *Int. J. Multiphase Flow*, Vol. 14, pp. 547-564.
- LeClair, B. P., and Hamielec, A. E., 1971, "Viscous Flow Through Particle Assemblages at Intermediate Reynolds Numbers-A Cell Model for Transport in Bubble Swarms," *Can. J. Chem. Eng.*, Vol. 49, pp. 713-720.

Levich, V. G., 1962, *Physicochemical Hydrodynamics*, Prentice-Hall, New York.

Martin, W. W. and Chandler, G. M., 1982, "The Local Measurement of the Size and Velocity of Bubbles Rising in Liquids," *Applied Scientific Research*, Vol. 38, pp. 239-246.

Moore, D. W., 1963, "The Boundary Layer on a Spherical Gas Bubble," *J. Fluid Mech.*, Vol. 16, pp. 161-176.

Morrison, F. A. Jr., and Stewart, M. B., 1976, "Small Bubble Motion in an Accelerating Liquid," *Trans. ASME, J. Appl. Mech.*, Vol. 43, pp. 399-403.

Odar, F., and Hamilton, W. S., 1964, "Forces on a sphere accelerating in a viscous fluid," *J. Fluid Mech.*, Vol. 18, pp. 302-314.

Rybczynski, W., 1911, *Bull. Int. Acad. Pol. Sci. lett., Cl. Sci. Math. Nat., Ser. A*, pp. 40-46.

Saffman, P. G., 1956, "On the Rise of Small Air Bubbles in Water," *J. Fluid Mech.*, Vol. 1, pp. 249-275.

Sellens, R.W., 1989, "A Derivation of the Phase Doppler Measurement Relations for an Arbitrary Geometry," *Experiments in Fluids*, Vol. 8, pp. 165-168.

Varty, R. L., 1986, "Fringe Method of Bubble Sizing Using a Laser Doppler Anemometer," *J. Phys. E: Sci. Instrum.*, Vol. 19, pp. 858-863.

Varty, R. L., 1991a, "Development of a Mathematical Model for a Bubble Rising above an Orifice," *Proceedings of the Thirteenth Canadian Congress of Applied Mechanics*, pp. 464-465.

Varty, R. L., 1991b, "An Algorithm for Processing Laser-Doppler Signals from Bubbles," *Proceedings of the Optical Sensing and Measurement Symposium, ICALEO'91* LIA Vol. 73, Laser Institute of America, Orlando, Florida, pp. 70-79.

Wallis, G. B., 1969, *One-dimensional Two-phase Flow*, McGraw-Hill, Inc.

Wallis, G. B., 1974, "The Terminal Speed of Single Drops or Bubbles in an Infinite Medium," *Int. J. Multiphase Flow*, Vol. 1, pp. 491-511.

APPENDIX A NOZZLE MAKING

Blanchard and Syzdek (1977) described a technique for manufacturing glass nozzles and they demonstrated that their nozzles produced bubbles of a specified size. Their technique was modified for the research reported here.

The nozzles required in this experiment can produce air bubbles of uniform size in water at a rate of about one per second. The nozzles are made from glass tubes of about 5.6 mm o.d., and 0.7 mm i.d. by heating and pulling them using an electromagnetic pulling machine manufactured by Narishige Scientific Instrument Laboratory, 4-27-9, Minami Karasoyama-cho Setagaya-ku, Tokyo, Japan. There are two procedures. The first is to pull a glass tube to a fine tip. The second is to polish the tip section until it is flat and about 90 degrees to the axis of the tip.

The pulling of the tips is done as two steps (see figure A.1). The first step consists of heating and pulling the tube to a fine taper by the magnetic pulling machine (a) and (b) and then reheating the tube at a point 45-55mm away from the beginning of the taper (c) and pulling simultaneously (c). When the tip breaks up from the upper part (d), the fine tip is made. The magnetic pulling machine was set up at 4 A on the magnetic meter and 7 A on the current meter.

The cutting of the tips is done by scribing the tips at the position desired with a disc with a diamond edge under a microscope and applying a bending and pulling force to break it up. Then the tip was polished on the polishing apparatus by gently holding the tip end. The polishing apparatus has a rotating disk with 8" in diameter covered by 400 silicon carbide grinding paper and was manufactured by Buehler Ltd., 2120 Greenwood St., Evanston., Illinois, USA.

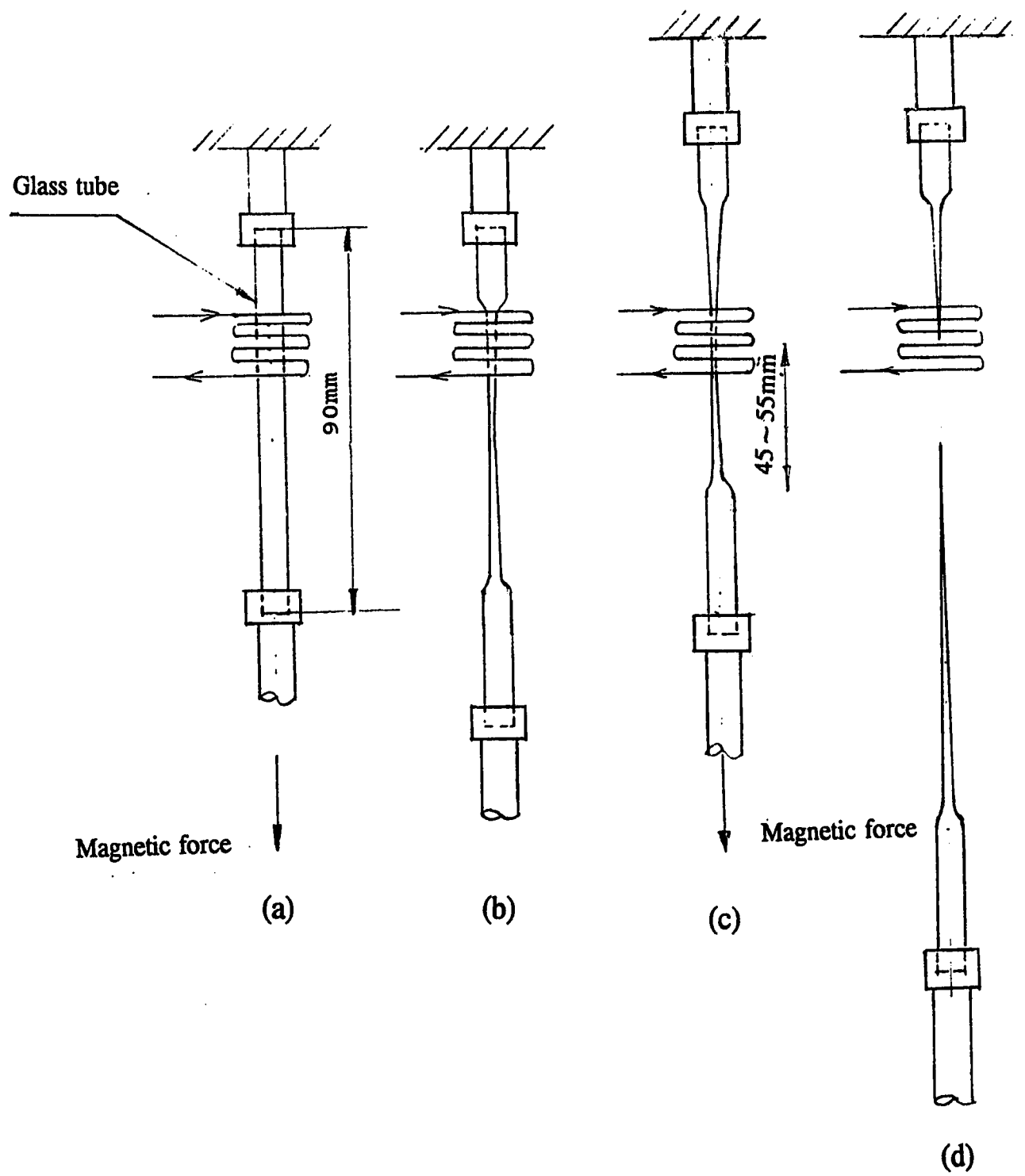


Figure A.1 The process of the pulling of the nozzle tip.

APPENDIX B TESTING THE LASER-DOPPLER ANEMOMETER

B.1 Testing the Opto-Electronic System

The LDA system was calibrated with a ~~model~~ spherical air bubble. The air bubble was embedded in a rectangular block of transparent silicone elastomer which was placed on the edge of a motor driven rotating vertical disk. The disk was then put on a top of the three-dimensional traversing mechanism. The model simulated a rising bubble moving through the LDA measuring volume. The linear velocity of the model air rising bubble can be determined by:

$$V_{dis} = 2\pi NR \quad (B.1.1)$$

where $R (= 0.0964 \text{ m})$ is the distance from the centre of rotation to the centre of the scattering sphere. N is the disk rotational speed (rps) which can be obtained accurately by placing the disk with several adjacent holes along a circle between a light and a detector. The light beam can only go through the disk and reach the detector to produce signals when the holes pass by. While the disk rotates one rotation, the light beam goes through the adjacent holes once and produces one set of signals. The time delay between two sets of signals on the oscilloscope is the time needed for the disk to rotate one cycle. Its reciprocal is the disk rotational speed.

The model air bubble linear velocity determined from the program LDAVEL (Varty, 1991b) is V_{pro} . The relationship between V_{dis} and V_{pro} (see figure B.1.1) is:

$$V_{dis} = (1.00 \pm 0.02)V_{pro} + (0.00 \pm 0.005) \quad (B.1.2)$$

which was used for calculating the experimental error bar.

B.2 Testing the Signal-Processing Program

The signal processing program was tested by finding the relationship between model bubble velocity calculated from the Doppler frequency from equation 3.3.2.1 and bubble velocity directly determined from the LDAVEL program. The velocity of the model air bubble was calculated from the equation below:

$$V_{osc} = \frac{f_D \times \lambda}{2 \times \sin \alpha} , \quad (B.2.1)$$

where: f_D is the Doppler frequency, which was obtained by counting the cycles and reading the time per division on the oscilloscope, λ ($=632.8 \times 10^{-9}$ m) is the wavelength of the laser beam in vacuum, α ($=5.532$ deg) is the half of beam intersection angle in vacuum.

The relationship between V_{osc} and V_{pro} (see figure B.2.1) is:

$$V_{osc} = (1.00 \pm 0.01) V_{pro} . \quad (B.2.2)$$

B.3 Bubble Size Measurement Using LDA

B.3.1 Introduction

In this appendix, two theories on which bubble size measurement using LDA is based are discussed. One theory is called the fringe method of particle sizing, first proposed by Durst and Zaré (1975). This theory involves the calculation of fringe spacing which is related to the surface curvature (or radius) of the scattering particle. The other theory is the Sellens' theory (Sellens, 1989) which is based on the measurement of the phase shift between two Doppler signals at different positions in space. It used the fact that the phase shift is related to the surface curvature of the particle.

Experiments were conducted using both model bubble specimens and real gas bubbles whose size was measured by photography. Using the above discussed two theories, the bubble size was calculated. Comparison was made of the bubble size between the calculated value and the actual or measured size.

B.3.2 Theories

B.3.2.1 The Fringe Method of Particle Sizing

The fringe method of particle sizing has been studied by Durst and co-workers

(Durst and Zaré, 1975; Durst, 1978,1982). The method was discussed and applied by Varty (1986).

The fringe spacing (d_f) for refraction of laser beams passing through the particle is given by Varty (1986):

$$d_f = \frac{L\lambda(m^{-1}-1)}{a \sin \alpha \cos(\frac{1}{2}\theta(m^{-1}-1)^{-1})} \quad (\text{B.3.1})$$

where (figure B.3.1(a)):

a is the radius of the bubble,

α is the half-angle of beam crossing,

m is the refraction index of the sphere relative to the surrounding medium,

θ is the scattering angle,

λ is the wavelength of the laser beam,

L is the distance between the centre of the sphere and the photodetector.

From equation 3.3.2.1, we obtain the bubble crossing velocity U_b as:

$$U_b = f_D \frac{\lambda}{2 \sin \alpha} . \quad (\text{B.3.2})$$

For a signal with a period of $T_D = 1/f_D$, the velocity at which the fringes cross the detector is:

$$V_f = \frac{d_f}{T_D} . \quad (\text{B.3.3})$$

When two detectors are separated by an effective distances S which is measured perpendicularly to the scattering direction in the vertical plane (figure B.3.1(b)), the time required for a fringe to move from detector 1 to detector 2 (T_s) is computed from the time delay between signal 1 (from detector 1) and signal 2 (from detector 2):

$$T_s = \frac{S}{V_f} . \quad (\text{B.3.4})$$

Substituting equation B.3.3 into equation B.3.4, yields

$$d_f = \frac{ST_D}{T_s} . \quad (\text{B.3.5})$$

From figure B.3.1(b), we have $S = S_o \sin \theta_s$, where S_o (=5.05 mm in the present case) is the distance between detectors 1 and 2. θ_s is the angle of the photodetector pair turned relative to the horizontal plane. Therefore,

$$d_f = \frac{S_o \sin \theta_s T_D}{T_s} \quad (\text{B.3.6})$$

where T_D and T_s can be obtained from the oscilloscope (T_D can also be calculated from equation B.3.2 if U_b is known). For a given θ_s and a given U_b (or T_D), only one value of T_s can be measured from the oscilloscope. Once d_f is determined from equation B.3.6, the bubble radius (a) can be calculated from equation B.3.1. For small θ_s , we have $\sin \theta_s \approx \theta_s$, and equation B.3.6 can be written in the following form:

$$\frac{S_o T_D}{d_f} = \frac{T_s}{\theta_s} . \quad (\text{B.3.7(a)})$$

With the substitution of d_f from equation B.3.1, equation B.3.7(a) can also be written as:

$$\frac{a \sin \alpha \cos(\frac{1}{2} \theta (m^{-1} - 1)^{-1}) S_o T_D}{L \lambda (m^{-1} - 1)} = \frac{T_s}{\theta_s} . \quad (\text{B.3.7(b)})$$

B.3.2.2 Sellens' theory

Sellens' theory was based on the determination of phase shift between two

Doppler signals at different points in space to calculate the particle size (Sellens, 1989). It was derived for an arbitrary geometry, which means that the receiving system does not have to be symmetric about the plane normal to the plane of the sending system. In the present study, two detectors were used. The schematic diagram of the two reference beams passing through a bubble in water is shown in figure B.3.2(a). The illustration of a reference beam can be seen in figure B.3.2(b). The angles are defined as follows:

α_w is the half angle of the sending beam intersection in water,

β_w is the half angle of the receiving beam intersection in water,

B_{11} is the scattering angle for light from beam 1 striking detector 1,

B_{12} is the scattering angle for light from beam 1 striking detector 2,

B_{21} is the angle between the sending beam 2 and the scattering beam 1,

B_{22} is the angle between the sending beam 2 and the scattering beam 2.

Because of the symmetry, $B_{12} = B_{21} = \alpha_w - \beta_w$,

$$B_{11} = B_{22} = \alpha_w + \beta_w.$$

The half-angle of beam crossing in vacuum (α) is 5.532° . The half angle of the sending beam intersection in the continuous phase (water or silicone) is therefore:

$$\alpha_w = \sin^{-1}\left(\frac{n_d}{n_c} \sin \alpha\right), \quad (\text{B.3.8})$$

The half angle of receiving beam intersection in air is:

$$\beta = \tan^{-1}\left(\frac{\frac{S_o}{2} \sin \theta_s}{L}\right). \quad (\text{B.3.9})$$

The half angle of receiving beam intersection in the continuous phase (water or silicone) is:

$$\beta_w = \sin^{-1}\left(\frac{n_d}{n_c} \sin\left(\tan^{-1}\left(\frac{\frac{S_o}{2} \sin \theta_s}{L}\right)\right)\right). \quad (\text{B.3.10})$$

From Snell's law (Sellens, 1989), the striking angles A_{ij} ($i=1,2; j=1,2$.) are given:

$$A_{12}=A_{21}=\frac{\pi}{2}-\tan^{-1}\left(\frac{\left|\frac{1}{m}-\cos\frac{B_{12}}{2}\right|}{\sin\frac{B_{12}}{2}}\right) \quad (\text{B.3.11})$$

where m is the refraction index of the sphere relative to the surrounding medium.

The difference between the refracted path length and the reference path length is:

$$\Delta L_{12}=\Delta L_{21}=D_b\left(n_d\left(1-\frac{\sin^2 A_{12}}{m^2}\right)^{\frac{1}{2}}-n_c \cos A_{12}\right) \quad (\text{B.3.13})$$

$$\Delta L_{11}=\Delta L_{22}=D_b\left(n_d\left(1-\frac{\sin^2 A_{11}}{m^2}\right)^{\frac{1}{2}}-n_c \cos A_{11}\right) \quad (\text{B.3.14})$$

where n_d ($=1$) is the refractive index of air and n_c is the refractive index of the continuous phase (1.33 for water, 1.43 for silicone).

The phase shift between the two Doppler signals was given:

$$\Delta \phi_{12}=\frac{2\pi}{\lambda}(\Delta L_{12}+\Delta L_{21}-\Delta L_{11}-\Delta L_{22}) . \quad (\text{B.3.15})$$

It can be written in the time delay form in the present case:

$$T_s=\frac{T_D}{\lambda}(\Delta L_{12}+\Delta L_{21}-\Delta L_{11}-\Delta L_{22}) . \quad (\text{B.3.16})$$

Substituting ΔL_{ij} into equation B.3.12, we have:

$$T_s = \frac{2T_b D_b}{\lambda} \left(n_d \left(1 - \frac{\sin^2 A_{12}}{m^2} \right)^{\frac{1}{2}} - \left(1 - \frac{\sin^2 A_{11}}{m^2} \right)^{\frac{1}{2}} \right) - n_c (\cos A_{12} - \cos A_{11}) . \quad (\text{B.3.17})$$

When the positions of the sending system and detectors are known, the scattering angle between any combination of sending beam and receiving detector can be determined by basic trigonometry. A_{ij} can be calculated from equations B.3.11 and B.3.12. As mentioned, T_s and T_b can be obtained from experiments. Since all the other parameters in equation B.3.17 are known by now, the bubble diameter (D_b) can be calculated from the equation.

B.3.3 Experimental Apparatus

The experimental apparatus for bubble size measurement was similar to that used for bubble velocity measurement (see figure B.3.3). When the light passed through the transmitting optics into the flow column, it was received by a photodetector pair which was mounted on a rotatable housing. Then the signals from the detectors were transmitted to two low pass filters and then to a digital storage oscilloscope. From the oscilloscope, the phase difference or time delay between the two signals can be obtained.

Two different sizes of air bubble model specimens were used for testing the photodetector pair. They are spherical voids in a transparent silicone elastomer which were used to simulate an air bubble crossing the laser beams. The model specimen was mounted on the edge of a motor-driven rotating disk. The description of these models can be found in the paper by Varty (1986). These two model specimens with radius of 2.36 mm and 4.36 mm (in radius) have also been used for testing the opto-electronic system and the signal-processing program. More details about the model specimens can be found in Appendix B.1 and B.2.

B.3.4 The Testing Results

B.3.4.1 Fringe Spacing

For calibration purposes, the model bubble can be held still and the spacing of the produced interference fringe can be measured directly from a screen. This was conducted by placing the specimen on the edge of a rotatable disk and letting two laser beams cross the centre of the specimen. By adjusting the position of the specimen, the two scattered beams produce fringes on a screen at the detector location. About 40 fringes was counted and used to calculate the average fringe spacing. These measured values are compared with the theoretical values calculated from equation B.3.1 using $\theta=0^\circ$, $L=493\text{mm}$, as shown below,

Table B.3.1 Comparison fringe spacing between theory and measurement.

=====		
Fringe Spacing(d_f) mm		
Radius(a) mm	Measured	Theoretical
=====		
2.36 ± 0.06	0.85 ± 0.01	0.847 ± 0.02
4.36 ± 0.06	0.455 ± 0.04	0.456 ± 0.01

Therefore, the measured values of d_f agree very well with the calculated values.

B.3.4.2 Signal Properties and Bubble Size

For a model bubble with radius $a = 2.36\text{ mm}$, the signal period T_D from the oscilloscope is $2.28 \times 10^{-5}\text{ s}$. figure B.3.4 shows the experimental results of T_s versus θ_s . Due to the equipment error, when θ_s equals to 1 deg., time delay T_s is zero. In the two theories discussed in section B.3.2, when θ_s equals to zero, time delay T_s is zero. Therefore, from this plot, we obtain the experimental value of $dT_s/d\theta_s$ (the slope) expressed as $(dT_s/d\theta_s)_E$. The value of T_s/θ_s can also be calculated from the above mentioned two theories, namely, equation B.3.7(b) and equation B.3.17 (knowing the model bubble size, $a=2.36\text{ mm}$). The two calculated values are denoted as $(dT_s/d\theta_s)_F$ and $(dT_s/d\theta_s)_S$, because they come from the fringe method of particle sizing and Sellens' theories, respectively. Comparison of $dT_s/d\theta_s$ between the experimental value and the

calculated values gives a direct indication about the properties of the signals and consequently, the accuracy of the theories.

The bubble size can thus be calculated from either equation B.3.7(b) or equation B.3.17 from the LDA measurement of $(dT_s/d\theta_s)_E$. The respective calculated bubble radii are denoted as a_F (equation B.3.7(b)) and a_s (equation B.3.17). All the above calculated results are summarized in table B.3.2 :

Table B.3.2 Comparison of signal properties between theories and measurement and comparison of bubble sizes calculated from two different theories with the known model bubble size for the radius $a=2.36$ mm.

=====				
$a=2.36$ mm $T_D = 2.28 \times 10^{-5}$ s $\theta=0^\circ$ $L=452$ mm				
=====				
$(dT_s/d\theta_s)_E \times 10^5$	$(dT_s/d\theta_s)_F \times 10^5$	$(dT_s/d\theta_s)_s \times 10^5$	a_F	a_s
(s/rad)	(s/rad)	(s/rad)	(mm)	(mm)

13.92	14.95	14.78	2.21	2.22

It can be seen that the two calculated values for $dT_s/d\theta_s$ are very close. However, the percent deviations between the experimental value $(dT_s/d\theta_s)_E$ and the calculated values $\{(dT_s/d\theta_s)_F$ and $(dT_s/d\theta_s)_s\}$ are 7.4% and 6.2%, respectively. Similarly, the two calculated values for bubble radius are very close, but each results in a 6.4% and 5.9% error compared with the bubble size ($a=2.36$ mm).

Similar calculations are conducted for a model bubble size of $a=4.36$ mm, and the results are summarized in table B.3.3.

Table B.3.3 Comparison of signal properties between theories and measurement and comparison of bubble sizes calculated from two different theories with the known model bubble size for the radius $a=4.36$ mm.

=====

a=4.36 mm $T_D = 0.64 \times 10^{-5} \text{ s}$ $\theta=0^\circ$ L=452 mm				
=====				
$(dT_s/d\theta)_E \times 10^5$	$(dT_s/d\theta)_F \times 10^5$	$(dT_s/d\theta)_S \times 10^5$	a_F	a_S
(s/rad)	(s/rad)	(s/rad)	(mm)	(mm)

7.8	7.7	7.7	4.41	4.44

Real gas bubbles rising from the flow column were also used for the calibration. Three bubble sizes were tested, namely, $a=0.52 \text{ mm}$, 0.62 mm , 0.625 mm . The calculated results are shown in table B.3.4.

Table B.3.4 Comparison of signal properties between theories and measurement and comparison of bubble sizes calculated from two different theories with the photographically measured bubble sizes.

(a) $a=0.52 \text{ mm}$

a=0.52 mm $T_D = 1.30 \times 10^{-5} \text{ s}$ $\theta=0^\circ$ L=452 mm				
=====				
$(dT_s/d\theta)_E \times 10^5$	$(dT_s/d\theta)_F \times 10^5$	$(dT_s/d\theta)_S \times 10^5$	a_F	a_S
(s/rad)	(s/rad)	(s/rad)	(mm)	(mm)

1.95	2.68	2.58	0.38	0.39

(b) 0.625 mm

a=0.625 mm $T_D = 1.18 \times 10^{-5} \text{ s}$ $\theta=0^\circ$ L=452 mm				
=====				
$(dT_s/d\theta)_E \times 10^5$	$(dT_s/d\theta)_F \times 10^5$	$(dT_s/d\theta)_S \times 10^5$	a_F	a_S
(s/rad)	(s/rad)	(s/rad)	(mm)	(mm)

1.6	2.86	2.83	0.350	0.353
<hr/>				
(c) a=0.62 mm				
=====				
a=0.62 mm	T _D = 1.37 x 10 ⁻⁵ s	θ=0°	L=452 mm	
=====				
(dT _e /dθ _e) _E x10 ⁵	(dT _e /dθ _e) _F x10 ⁵	(dT _e /dθ _e) _S x10 ⁵	a _F	a _S
(s/rad)	(s/rad)	(s/rad)	(mm)	(mm)
<hr/>				
2.58	3.29	3.26	0.486	0.490
<hr/>				

It can be seen that in all the cases the two calculated values for $dT_e/d\theta_e$ are very close. However, the deviations between the experimental value $(dT_e/d\theta_e)_E$ and the calculated values $(dT_e/d\theta_e)_F$ and $(dT_e/d\theta_e)_S$ are quite larger. Similarly, the two calculated values for bubble radius are close. However, there is a larger difference between the calculated value and the measured bubble size by photography. In view of this apparent error of as much as 44.0%, this method was not used for bubble size measurement.

The discrepancy in bubble size measurement may be due to the fact that the gas bubble size is very small and the bubble is not able to scatter enough light, because a smaller error is involved in the case of model bubble calibration, where the bubble sizes are relatively larger.

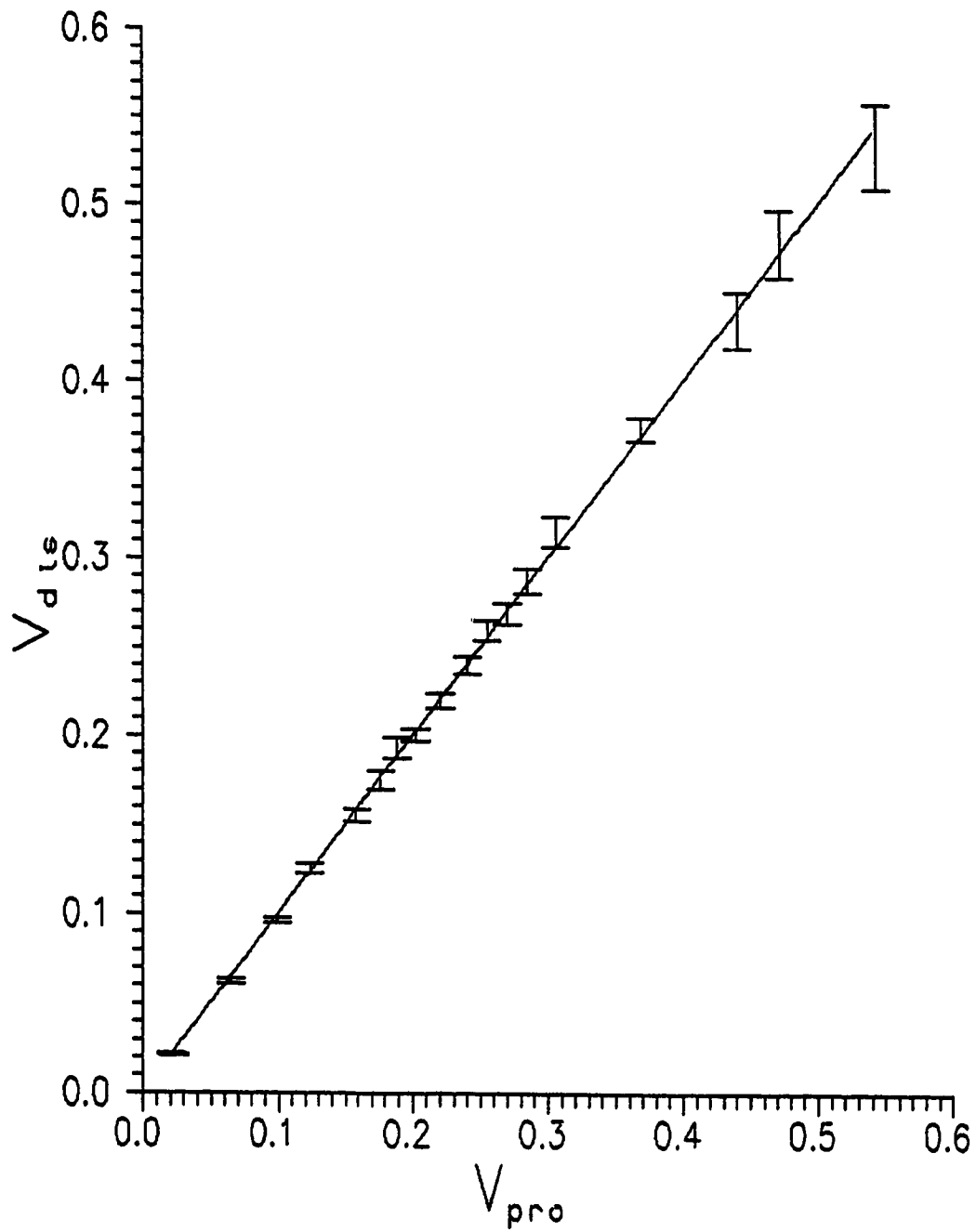


Figure B.1.1 Variation of the model air bubble rising velocity (calculated from the rotating speed of the disk) with the model air bubble rising velocity (measured from the LDAVEL program).

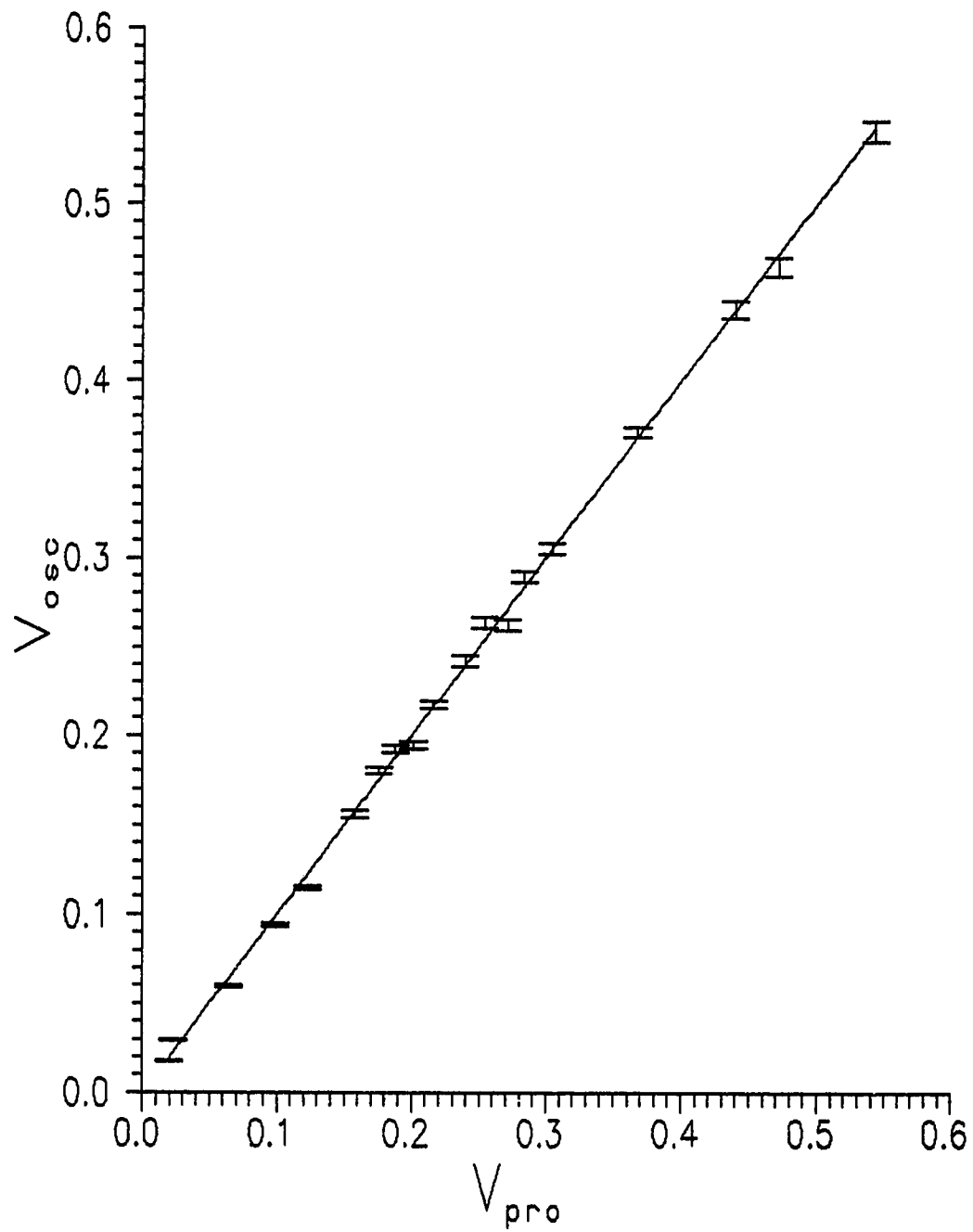


Figure B.2.1 Variation of the model air bubble rising velocity (calculated from the signal frequency) with the model air bubble rising velocity (measured from the LDAVEL program).

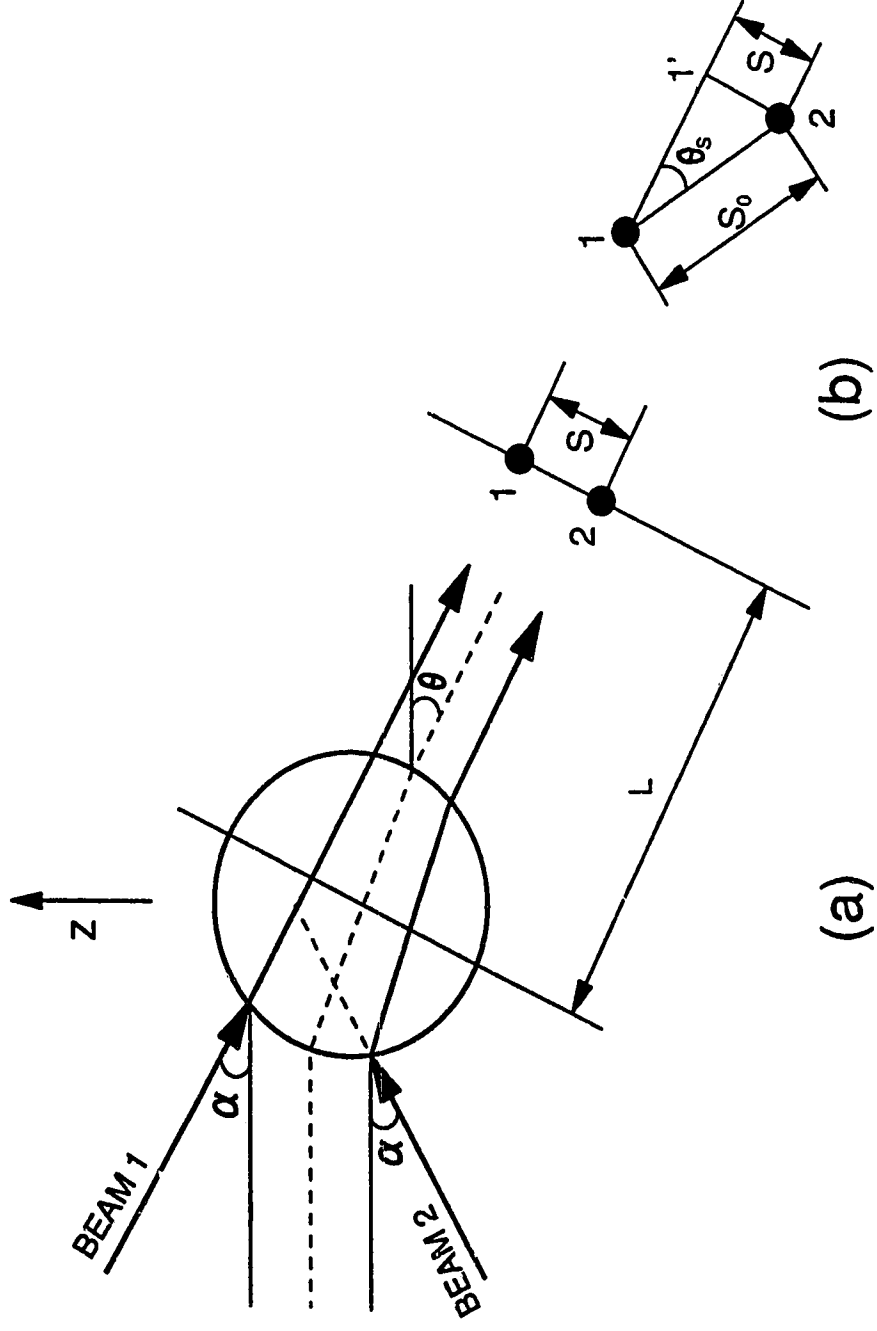


Figure B.3.1 (a) Two crossing laser beams passing through a bubble, (b) received by a photodetector pair.

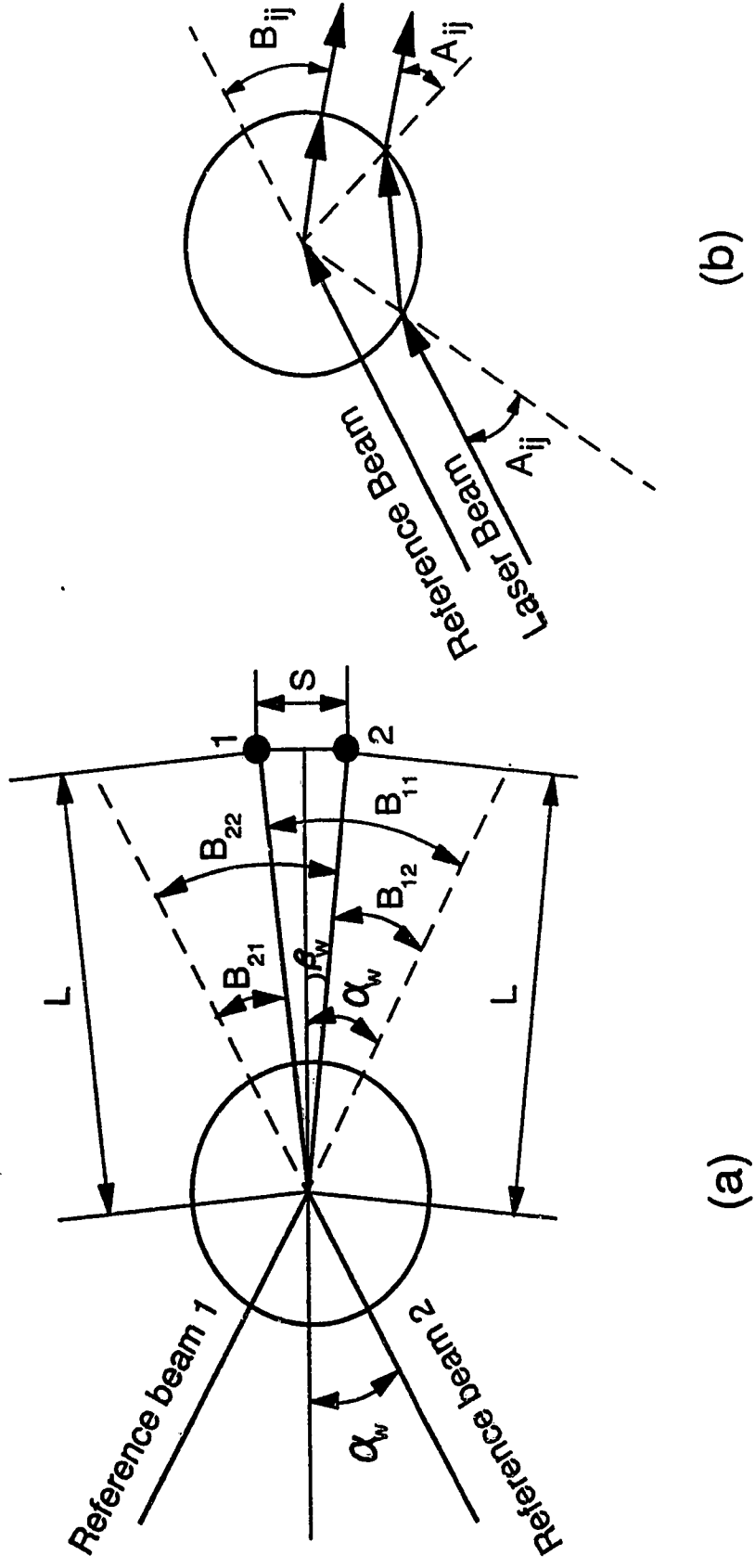


Figure B.3.2 (a) Two reference beams passing through a bubble in water, (b) scattering by refraction in a bubble.

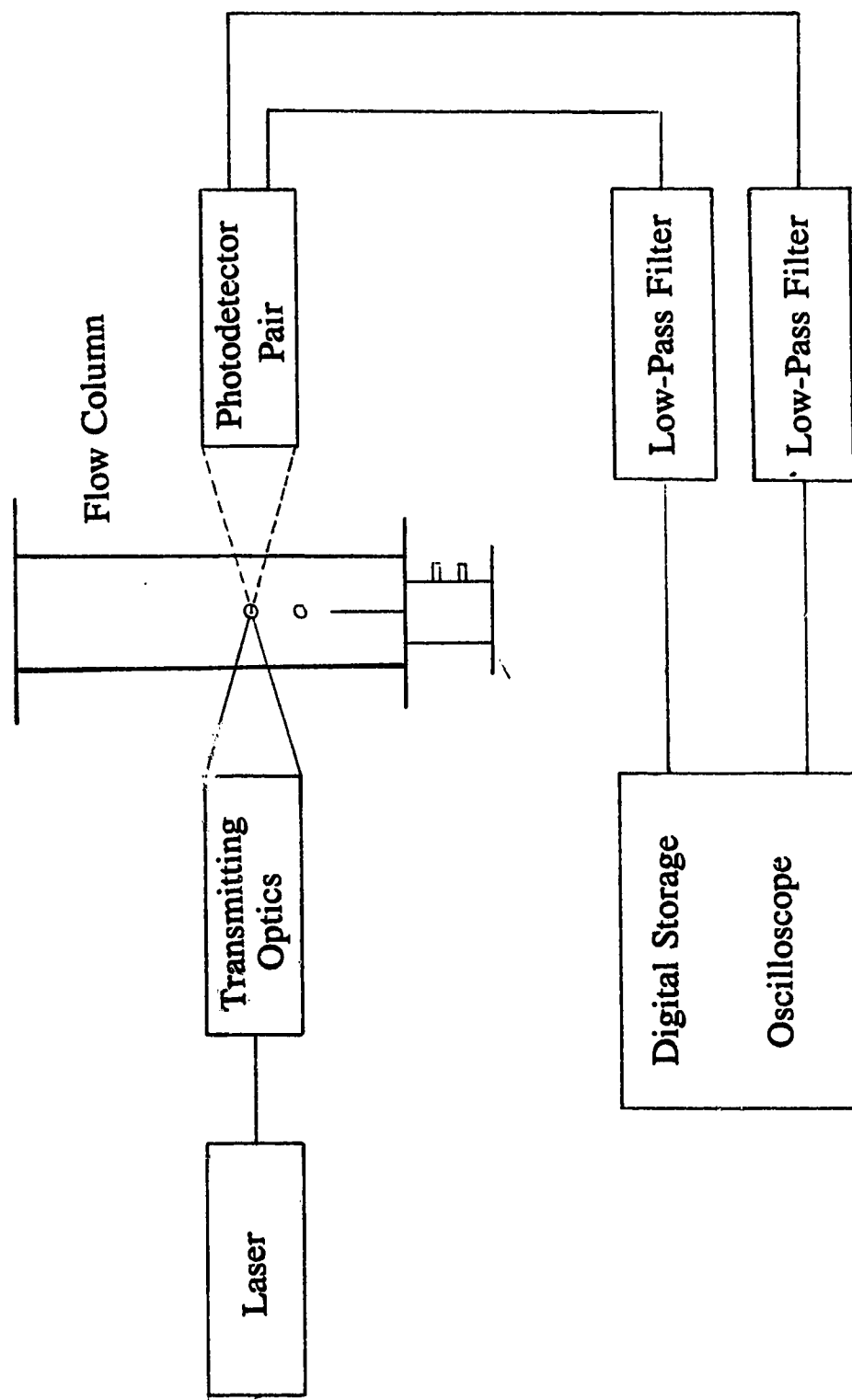


Figure B.3.3 Flow column and laser-Doppler anemometer for bubble size measurement.

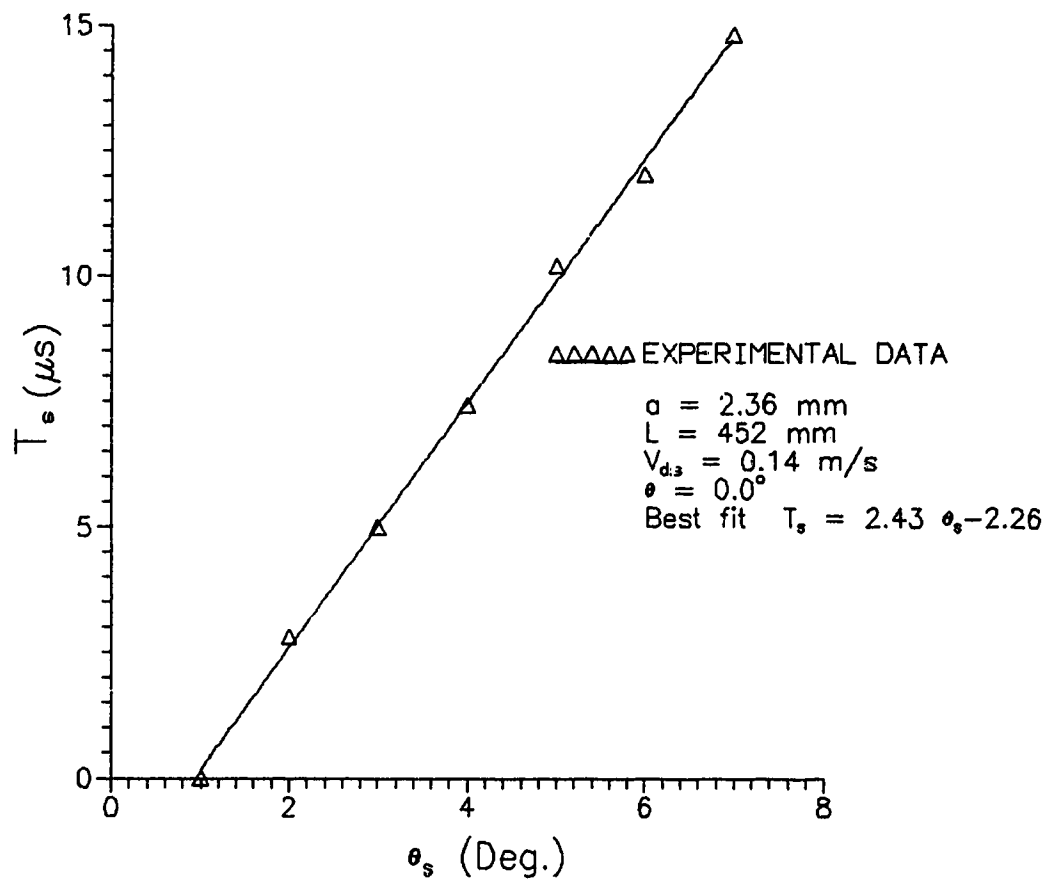


Figure B.3.4 Variation of time delay with photodiode orientation (turning angle).

APPENDIX C DETERMINATION OF THE DIMENSIONLESS GROUPS

Two dimensionless groups were used for correlating experimental data in Chapter 4. One dimensionless group $(z_b - z_{bo})g/U_{bT}^2$ was derived by Dr. Varty in one of our meetings. It is based on the analytic solution of spherical-bubble motion using $C_D = K/Re$ derived by Varty (1991a), which can be written as:

$$\frac{(z_b - z_{bo})K_1^2}{-(\rho_b + \frac{\rho}{2})V} = K_1 U_b + (\rho - \rho_b)Vg \ln\left(1 - \frac{K_1}{(\rho - \rho_b)Vg} U_b\right) \quad (C.1)$$

where $K_1 = K\pi\mu D_b/8$.

The terminal velocity of a spherical bubble can be derived from equation 4.7.1 using $C_D = K/Re$:

$$U_{bT} = \frac{(\rho - \rho_b)Vg}{K_1} \quad (C.2)$$

and equation C.2 can also be written as:

$$(\rho - \rho_b)Vg = K_1 U_{bT} \quad (C.3)$$

Substituting equation C.3 into equation C.1, we obtain:

$$\frac{(z_b - z_{bo})K_1^2}{-(\rho_b + \frac{\rho}{2})V} = K_1 U_b + K_1 U_{bT} \ln\left(1 - \frac{U_b}{U_{bT}}\right) \quad (C.4)$$

Substituting K_1 from equation C.3 and rearranging yields:

$$\frac{z_b - z_{bo}}{U_{bT}^2} \frac{(\rho - \rho_b)g}{(\rho_b + \frac{\rho}{2})} = -\frac{U_b}{U_{bT}} - \ln\left(1 - \frac{U_b}{U_{bT}}\right) \quad (C.5)$$

For $\rho \gg \rho_b$, equation C.5 becomes:

$$2 \frac{(z_b - z_{bo})g}{U_{bT}^2} = -\frac{U_b}{U_{bT}} - \ln\left(1 - \frac{U_b}{U_{bT}}\right) \quad (\text{C.6})$$

therefore, U_b/U_{bT} and $(z_b - z_{bo})g/U_{bT}^2$ appear to be relevant dimensionless groups. $(z_b - z_{bo})g/U_{bT}^2$ can also be written as $\rho(z_b - z_{bo})/(\Delta\rho D_b Fr)$ which again can be approximated as $(z_b - z_{bo})/(D_b Fr)$ (in the present study, D_e was used because the bubble shapes are close to spherical), where Fr is the Froude number which was defined in section 2.1, based on U_{bT} . Alternatively, $(z_b - z_{bo})g/U_{bT}^2$ could be described as the inverse Froude number based on U_{bT} and $(z_b - z_{bo})$.